Mechanism of SK2 channel gating and its modulation by the bee toxin apamin and small molecules

Samantha J. Cassell[1,5], Weiyan Li[2,5], Simon Krautwald[3], Maryam Khoshouei[4], Yan Tony Lee[2], Joyce Hou[2], Wendy Guan[2], Stefan Peukert[3], Wilhelm A. Weihofen[1], Jonathan R. Whicher[1,6]

1. *Discovery Sciences, Novartis Biomedical Research, 250 Massachusetts Avenue, Cambridge, MA 02139, United States*
2. *Cardiovascular and Metabolism, Novartis Biomedical Research, 22 Windsor Street, Cambridge, MA 02139, United States*
3. *Global Discovery Chemistry, Novartis Biomedical Research, 181 Massachusetts Avenue, Cambridge, MA 02139, United States*
4. *Discovery Sciences, Novartis Biomedical Research, Novartis Pharma AG, Basel, Switzerland*
5. *These authors contributed equally*
6. *Corresponding author jonathan.whicher@novartis.com*

Abstract

Small-conductance calcium-activated potassium channel 2 (SK2) serves a variety of biological functions by coupling intracellular calcium dynamics with membrane potential. SK2 modulators are in development for the treatment of neurological and cardiovascular diseases, though the mechanisms of pharmacological modulation remain incompletely understood. We determined structures of an SK2-4 chimeric channel in Ca^{2+}-bound and Ca^{2+}-free conformations and in complex with the bee toxin apamin, a small molecule inhibitor, and a small molecule activator. The structures revealed that the S3-S4 linker forms a hydrophobic constriction at the extracellular opening of the pore. Apamin binds to this extracellular constriction and blocks the exit of potassium ions. Furthermore, we identified a structurally related SK2 inhibitor and activator that bind to the transmembrane domains. The compounds exert opposing effects on gating by differentially modulating the conformation of the S6 helices. These results provide important mechanistic insights to facilitate the development of targeted SK2 channel therapeutics.

Introduction

Fundamental to a variety of biological processes, ion channels are an important class of therapeutical targets. Small conductance calcium-activated potassium (KCa2.x, or SK1, 2, and 3) channels are activated by increased intracellular Ca^{2+} to induce potassium efflux and regulate membrane potential[1-3]. In this role, SK1, 2, and 3 mediate cellular excitability and have different but overlapping functions in many cell types including neurons, endothelial cells, and cardiomyocytes[4]. In particular, the SK2 channel regulates

synaptic transmission and plasticity, learning and memory, and cardiac action potentials and thus has attracted attention as a potential target for the treatment of neurological and cardiovascular diseases[2,5,6]. SK2 activators reduce cellular excitability and are potential therapeutics for alcohol dependence[7], ataxia[8], epilepsy[9], and stroke[10]. Conversely, SK2 inhibitors increase cellular excitability and have been proposed for the treatment of Alzheimer's disease[11] and atrial fibrillation[12].

The cryo-EM structure of the related SK4 (KCa3.1, IK) channel provided the first insights into the architecture and mechanism of Ca^{2+}-dependent gating for the SK channel family[13]. SK4 channels form non-domain swapped tetramers, with each subunit containing six transmembrane helices S1 to S6[1,13]. S1-S4 form a voltage-sensor like domain where the S4 helices lack the positively charged residues necessary for voltage sensitivity. The S5 and S6 form the potassium pore. Within the potassium pore lies the selectivity filter, a structure unique to potassium channels that is required for rapid and selective conductance of K^+ ions[14]. Following the S6 helices there are two intracellular helices (HA and HB) that form the binding site for the Ca^{2+}-binding protein calmodulin (CaM), which acts as the Ca^{2+} sensor to gate SK channels[15]. The CaM C-lobe is constitutively bound to the HA and HB helices, and upon an increase in intracellular Ca^{2+} the CaM N-lobe binds to a unique S4-S5 linker, inducing a conformational change in the S6 helices to open the potassium pore and activate the channel[13].

SK2 activators described to date bind at the interface of the CaM N-lobe and S4-S5 linker and function by stabilizing this interaction[13,16,17]. On the other hand, known SK2 inhibitors target the extracellular and/or transmembrane regions and were proposed to function by either direct pore block or negative gating modulation[16]. The binding site for the bee venom toxin apamin, a cyclic 18 residue peptide inhibitor, has been mapped to the extracellular loop regions of SK2[18-20]. Apamin is of historical importance as it was used to elucidate the physiological role of SK2 and apamin inhibition of SK2 increases neuronal excitability and improves learning and memory [3,21]. Apamin inhibits SK1, 2, and 3 but not 4, and is most potent against SK2 with an IC_{50} of ~70 pM[1,22]. Functional mutagenesis of apamin identified two arginine residues that are essential for inhibition[23]. Mutagenesis experiments on the SK2 channel indicated that residues in the extracellular loops between S3 and S4 (S3-S4 linker) and between S5 and S6 are important for apamin binding and inhibition[18-20]. Since the S3-S4 linker is predicted to be distant to the pore an allosteric mechanism of apamin inhibition rather than a direct pore block has been suggested[20]. Attempts to recapitulate the potency and selectivity of apamin with small molecules resulted in the development of a class of inhibitors, such as UCL1684, that are predicted to have an overlapping binding site with apamin[24-26]. These small molecules generally carry two positive charges, which may mimic the two arginine residues in apamin that are essential for inhibition[23]. Further characterization of the molecular mechanisms of inhibition by apamin and the small molecule pore blockers is

required to understand how the interaction between the S3-S4 linker and the essential arginine residues/positive charges block ion conduction in SK2.

Another class of small molecule SK2 inhibitors act as negative gating modulators by shifting the Ca^{2+} dependence of activation to higher Ca^{2+} concentrations[27,28]. One such inhibitor, AP31969, is currently in clinical trials for the treatment of arrhythmia[29]. Mutagenesis experiments with the structurally-related inhibitor AP14145 suggest that these compounds bind within the pore directly below the selectivity filter[28]. Similar potencies on SK1, 2, and 3 channels have been reported most likely due to the homology of pore lining residues in the SK family. However, selective SK1 inhibitors were developed that take advantage of a unique residue, Ser293, on S5[30]. Interestingly, only small modifications to this family of inhibitors are sufficient to switch the activity profile from inhibition to activation of SK1. However, it remains unclear how compounds that bind the transmembrane regions of SK channels affect Ca^{2+}-dependent gating, which is driven by the interaction between CaM and the intracellular domains.

Despite SK2 being a prominent therapeutic target for both neurological and cardiovascular diseases, no structure of human SK2 has been reported to date. The sequence for the transmembrane domains of SK2 differ significantly from those of SK4, which limits the potential of the existing SK4 structures in understanding the molecular mechanisms of SK2 pharmacological modulation. To enable high-resolution cryo-EM studies of human SK2, we designed a chimera (SK2-4) that contains the transmembrane and extracellular domains of human SK2 and intracellular domains of human SK4. The structures of the SK2-4/CaM complexes in the Ca^{2+}-bound and Ca^{2+}-free conformations demonstrate that SK2 and SK4 adopt similar overall architectures and share a similar mechanism for Ca^{2+}-dependent gating. However, unlike SK4, we observed a structured S3-S4 linker that induces a conformational change in the selectivity filter and forms a hydrophobic constriction at the extracellular opening of the SK2 pore. Apamin binds to the extracellular constriction formed by the S3-S4 linker to block potassium efflux. In addition, high throughput screening and medicinal chemistry optimization efforts yielded a new class of potent SK2 inhibitors that bind to a novel pocket formed by the S5, S6, and pore helices and induce closure of the S6 helices. Structure-guided design efforts enabled switching the activity profile towards activation while retaining the same binding mode. The detailed understanding of two distinct mechanisms of SK2 channel inhibition, extracellular pore block and negative gating modulation, and a new mechanism for channel activation presented here should facilitate the rational design of potent and selective SK2 modulators.

Results

Characterization of the SK2-4 chimeric channel

We attempted to solve the structure of wild-type (WT) human SK2 (Fig S1) expressed and purified from mammalian cells in the presence of CaM and Ca^{2+}. However, 2D class

averages showed disorder in the intracellular region (Fig S2A). Subsequent 3D reconstruction generated a low-resolution, anisotropic map for the transmembrane helices and no interpretable density for the intracellular domains.

The SK4 channel cryo-EM structure suggested that the intracellular regions of SK4 may be more rigid than those of SK2[13]. We hypothesized that the SK4 intracellular domains would remain ordered when fused to the SK2 TM domains. A chimeric construct was created with the goal of preserving all transmembrane and extracellular regions of human SK2 while replacing the N- and C-terminal intracellular regions with those of human SK4 (Fig 1A, S1, and methods for details). Within the intracellular regions, only the N-terminal portion of the HA helix (residues 401-412 in SK2) that was predicted to interact with the S4-S5 linker retained the SK2 sequence[13].

To confirm that SK2-4 behaves similarly to the WT SK2 channel, we conducted functional and pharmacological characterization (Fig 1B,C,D). Electrophysiological measurements demonstrated that SK2-4 current has a similar reversal potential as WT SK2 and SK4 currents (Fig 1B), which is near the expected value for a K^+-selective channel based on the K^+ concentration gradient. Like WT SK2 and SK4, the activation of SK2-4 is dependent on intracellular Ca^{2+} concentration (Fig 1C). The Ca^{2+} sensitivity of SK2-4 is higher than that of SK2 but similar to SK4, consistent with the CaM binding domain of the chimera stemming from SK4. In addition, SK2-4 activity was inhibited by known SK2 inhibitors apamin and AP14145 with an IC_{50} of 0.7 nM and 2.4 μM, respectively (Fig 1D). Of note, neither of these inhibitors is active against the WT SK4 channel, indicating that key regions of the SK2 native structure are preserved in the chimera[22,28]. We also tested dozens of other available SK2 inhibitors of diverse scaffolds and observed a close correlation between potency on WT SK2 and the SK2-4 chimera (data not shown). Given the high degree of agreement between our characterization and previously reported data, we are confident that the SK2-4 chimeric channel recapitulates the native activity and transmembrane architecture of WT SK2.

Structure of SK2-4/CaM in Ca^{2+}-bound and Ca^{2+}-free states

SK2-4 was co-expressed with CaM and purified from mammalian cells in the presence of Ca^{2+}. The cryo-EM structure was determined to a final resolution of 3.1 Å with most regions of the structure well-defined by density apart from the C-terminal HC helical bundle (Fig 2A, S2, S3A, Table 1). Residue numbers in the SK2 regions of the structure correspond to the human SK2 sequence described by Desai *et al.* [31] and the SK4 regions of the structure are numbered sequentially from the SK2 regions (Fig 1A).

SK2-4/CaM forms a non-domain swapped tetramer with four CaM molecules bound, similar to the previously reported SK4/CaM structure[13] (Fig 2A). In the presence of Ca^{2+}, the C-lobe of each CaM is bound to the HA and HB helices and the N-lobe is bound to a short helix in the S4-S5 linker, $S_{45}A$, on the neighboring subunit (Fig S2G,H). The

measured SK2-4 pore radius (3.8 Å) indicates that the S6 helices are in an open conformation in the presence of Ca^{2+} (Fig 2C,D).

We also purified SK2-4/CaM in the absence of Ca^{2+} and determined the cryo-EM structure at 3.4 Å (Fig 2B, S2, S3B, Table 1). In the structure, there is clear density for the S1-S6 regions but as observed in the closed conformation of SK4, the CaM density is weak and the N-lobes of CaM are dissociated from the $S_{45}A$ helices[13]. Furthermore, the $S_{45}B$ and S6 helices collapsed around the pore axis and the pore is closed with a radius of 1 Å at the intracellular gate at Val390 (Fig 2C,D). The structures of SK2-4/CaM in the Ca^{2+}-bound and Ca^{2+}-free conformations confirm that the chimeric channel is gated by Ca^{2+} and that the mechanism of channel gating is similar to that of SK4.

S3-S4 linker structure

Although SK2-4 and SK4 share similar overall architecture, there are notable differences in the SK2 portion spanning the S1-S6 transmembrane region. The extracellular S3-S4 linker is not visible in the structure of SK4, indicating flexibility and lack of defined structure[13]. In contrast, the S3-S4 linker of SK2-4 is well-defined by density in both the Ca^{2+}-bound and Ca^{2+}-free structures and forms a two-stranded anti-parallel β-turn (residues Gly231-Asp253) that extends over the S5 and S6 helices (Fig 3, S3A,B). The β-turn interacts with residues Tyr335 and His336 at the C-terminus of the S5 helix (Fig 3B). His336 forms an edge-to-face interaction with Trp237 and a hydrogen bond with Ser248, whereas Tyr335 forms a hydrogen bond with Asp253. The β-turn features an eight amino acid loop (residues 240-247) that extends into the potassium pore (Fig 3C, 4A, S4A,B). Arg240, Phe243, and Tyr245 within this loop form direct interactions with residues at the C-terminus of the selectivity filter. Arg240 and Tyr245 form a salt bridge and hydrogen bond with the side chain and backbone of Asp363 from a neighboring subunit, respectively. Phe243 extends into the ion conduction path and is within C-H/O bonding distance to the backbone carbonyl of Gly362 (Fig 3C). In this position, the four Phe243 residues form edge-to-face interactions that create a hydrophobic constriction at the extracellular opening of the pore with a radius of 1.8 Å, which is expected to prohibit efflux of hydrated K^+ ions measuring 6 Å in diameter (Fig 2D, 3A, 4A). Therefore, even though the intracellular gate at Val390 is open in the SK2-4/CaM Ca^{2+}-bound structure, the observed conformation is expected to be non-conductive. For conduction to occur, a structural rearrangement of the S3-S4 linker that increases the diameter of the extracellular constriction would be required.

All residues participating in interactions between the S3-S4 linker and the pore resides are fully conserved in SK1, 2, and 3 (Fig S1), suggesting that S3-S4 linker conformation is an important structural feature of the SK channels. In addition, the S3-S4 linker conformation is important for apamin inhibition as mutation of Tyr245 and His336, which are involved in hydrogen-bonding interactions between the S3-S4 linker and pore residues, reduce apamin potency[19,20].

Selectivity filter conformation

The selectivity filter is a crucial component of all selective K^+ channels, including SK4. It contains the highly conserved (T/S)XG(Y/F)G motif, where the T/S hydroxyl and the backbone carbonyls of subsequent residues form four consecutive K^+ coordination sites that perfectly mimic the hydration shell of a K^+ ion (Fig 4B,C) [14,32]. Extensive structural and mechanistic studies demonstrated that this selectivity filter structure is required for the fast and selective conduction of K^+ ions[33-37]. Reducing the number of K^+ coordination sites in the selectivity filter to two produces channels that are no longer K^+ selective and behave similarly to non-selective cation channels like HCN or NaK, that can pass Na^+ in addition to K^+[35,38].

In the structures of SK2-4/CaM in both the Ca^{2+}-bound and Ca^{2+}-free conformations, Tyr361, located in the center of the selectivity filter, is rotated approximately 180° when compared with the homologous Tyr253 in SK4 (Fig 4A,C,D, S4A,B)[13]. In addition, the backbone carbonyls of Gly360 and Tyr361, which typically form the extracellular K^+ coordination sites one and two, are rotated away from the center of the selectivity filter and the ion conduction path. As a result, only the two intracellular K^+ coordination sites, three and four, are intact and occupied by K^+.

SK2 and SK4 selectivity filters were predicted to adopt similar conformations based on sequence conservation in the selectivity filter and surrounding residues (Fig S1). Therefore, the conformation of the selectivity filter observed in the SK2-4 structure is likely due to the S3-S4 linker, which is disordered in SK4. As discussed above, Asp363 at the C-terminus of the selectivity filter is directed towards the extracellular S3-S4 linker and interacts with Arg240 and Tyr245 (Fig 3C, 4A, S4A,B). In SK4, the homologous aspartate (Asp255) is directed towards the pore helix and forms a hydrogen bond with a conserved tryptophan (Trp242) (Fig 4C)[13]. The homologous pore helix tryptophan in SK2, Trp350, adopts a different rotamer and is unable to form a hydrogen bond with Asp363 (Fig 4A, S3A,B). The hydrogen-bonding interaction between a pore helix residue (usually Trp or Tyr) and the residue at the C-terminus of the selectivity filter (usually Asp or Asn) is a conserved feature of K^+ selective channels[37]. Furthermore, inserting this interaction into non-selective channels produces K^+ selective channels with four K^+ coordination sites, while deletion of this interaction from K^+ selective channels produces non-selective channels with two K^+ coordination sites[36,37]. Therefore, we propose that by interacting with Asp363 and thereby preventing its interaction with the pore helix Trp350, the S3-S4 linker induces the selectivity filter conformation observed in SK2-4 with two K^+ coordination sites. We predict that the SK1 and 3 selectivity filters could adopt similar conformations with two K^+ coordination sites because the S3-S4 linker residues that interact with Asp363 are conserved among these channels (Fig S1).

Except for one report indicating significant sodium permeability in rat SK2[39], studies show that SK2 is K^+ selective[1,31,40,41]. The reversal potential of SK2 and SK2-4

presented here confirms K^+ selectivity (Fig 1B). This contrasts with the SK2-4 structures as selectivity filters with two K^+ coordination sites are predicted to be non-selective[35-38]. However, the Ca^{2+}-bound SK2-4/CaM structure is in a non-conductive conformation, despite the open intracellular Val390 gate, due to Phe243 of the S3-S4 linker forming a constriction at the extracellular opening that prevents K^+ efflux. Thus, the selectivity filter conformation should not affect the K^+ selectivity observed in the experimental data[1,31,40,41].

Mechanism of apamin inhibition

Extensive mutational studies suggest that the SK2 S3-S4 linker is essential for apamin binding and inhibition, although the nature of their interaction remains unknown[18,19]. To understand how apamin interacts with the unique conformation of the S3-S4 linker and how that interaction inhibits K^+ conduction, we incubated Ca^{2+}-bound SK2-4/CaM with excess apamin prior to cryo-EM grid preparation. 3D reconstruction in C4 symmetry produced a map with additional density at the extracellular opening of the K^+ pore consistent with the size of a single apamin molecule bound per tetramer. However, the C4 symmetric density corresponds to asymmetric apamin bound to four distinct but structurally equivalent orientations, which prevented apamin fitting. To more accurately align particles and improve the apamin density we used a combination of focused classification and local refinements to generate a reconstruction in C1 symmetry to a final resolution of 3.2 Å (Fig S3C, S5, Table 1). Elongated density in the C1 map at the extracellular opening of the pore allowed for accurate placement of the C-terminal helix (residues 6-17) from an NMR structure of apamin (Fig 5A)[22]. Two well-defined tubular densities at the center of the helix were confidently modeled with the side chains of Arg13 and Arg14.

Overall, the apamin-bound SK2-4/CaM structure resembles the Ca^{2+}-bound conformation. The N-terminal lobe of CaM engages with the $S_{45}A$ helix and the S6 helices are in an open conformation (Fig 2D). The C-terminal helix of apamin binds at the extracellular opening of the pore and interacts with all four S3-S4 linkers of the tetramer (Fig 5A). Essential residues Arg13 and Arg14 insert into the Phe243 constriction to form cation-π interactions (Fig 5A,C) [23]. In this position, apamin blocks the exit of K^+ ions from the extracellular side of the pore to inhibit conduction.

To probe the interaction between SK2 Phe243 and apamin Arg13 and Arg14 we determined the apamin sensitivity of a Phe243Ala mutant and found it to be insensitive to apamin inhibition up to 3 μM (Fig 5B), demonstrating the critical role of this interaction for apamin binding and inhibition. Prior mutagenesis of both the S3-S4 linker and the outer pore regions further support the observed apamin binding site and proposed mechanism of apamin inhibition. For example, mutation of Ser244 and Tyr245 in the S3-S4 linker reduce the potency of apamin by 10-fold and 5-fold, respectively[18,19]. Ser244 is within 5 Å of the apamin binding site and bulky mutations may clash with apamin (Fig

5A). Tyr245 hydrogen bonds with Asp363 likely stabilizing the S3-S4 linker conformation for apamin binding (Fig 3C). In the outer pore, mutation of His336 decreases sensitivity of SK2 to apamin[20]. As discussed above, this residue also stabilizes the S3-S4 linker conformation (Fig 3B). Notably, the previous mutagenesis experiments decreased but did not fully abolish the potency of apamin as we observed for the Phe243Ala mutation underscoring that the interaction between apamin and Phe243 is essential.

Fortuitously, the apamin-bound structure provides some insight into S3-S4 linker dynamics and the potential transition from a closed to open extracellular constriction. Insertion of apamin Arg13 and Arg14 dilates the Phe234 constriction from 1.8 Å to 3 Å (Fig 2D and 5C). Such a S3-S4 linker conformation in the absence of apamin, would permit K^+ ion conduction, providing an understanding of the type of S3-S4 movement required to expand the extracellular constriction. Compared with the apamin-free Ca^{2+}-bound conformation (Fig 4A), the movement of the S3-S4 linker away from the pore axis upon apamin binding is accompanied by multiple conformational changes in the selectivity filter to adopt the canonical K^+-selective conformation with four K^+ coordination sites: Arg240 withdraws and frees Asp363 to form a weak hydrogen bond with a rotated Trp350 side chain while Tyr361 in the selectivity filter is rotated 180° (Fig 5C,D and S4C). Therefore, we hypothesize that in the conductive/dilated state of the extracellular constriction, the S3-S4 linker and Phe243 withdraw from the pore axis and the selectivity filter returns to the canonical conformation with 4 K^+ coordination sites to maintain the K^+ selectivity demonstrated for SK2[1,31,40,41].

Identification and functional characterization of novel SK2 modulators

To identify new modulators of SK2 we developed a high throughput patch clamp assay using the Qube system (Sophion) (see methods section for details). Small molecule library screening and subsequent rounds of medicinal chemistry optimization produced compound 1 as a potent inhibitor of SK2 with an IC_{50} of 69 nM (Fig 6A,B). Selectivity profiling demonstrated that compound 1 has a 10-fold reduced potency for SK4 (IC_{50} of 660 nM) but is selective over other ion channels tested including hERG, Nav1.5, KCNQ1, and Cav1.2 (Fig 6B, S6A). Compound 1 inhibits SK2-4 chimera with similar potency as WT SK2 (Fig 6B), suggesting binding at the transmembrane or extracellular domains. Furthermore, we used differential scanning fluorimetry (DSF) to confirm binding of compound 1 to SK2-4. Addition of compound 1 resulted in a strong thermal stabilization of 10.8 °C, indicative of target engagement (Fig 6C).

To characterize the mechanism of inhibition, we determined the co-structure of compound 1 bound to SK2-4/CaM in the presence of Ca^{2+} at 3.3 Å resolution (Fig S3, S5, Table 1). Four molecules of compound 1, which is clearly defined by cryo-EM density, were bound per SK2-4 tetramer at the interface of the S5, pore helix, and S6 of each subunit (Fig 6D,E). The benzoxadiazole moiety of compound 1 rests in a hydrophobic pocket lined by Leu321 and Ala325 of S5, Ile352 and Phe356 of the pore

helix, and Met381 of S6. In the Ca^{2+}-bound and Ca^{2+}-free apo conformations of SK2-4/CaM this pocket is blocked by Leu321 adopting an alternative rotamer conformation (Fig S6B,C,D). The central benzamide moiety is positioned between Trp322 of S5 and Phe356 and Leu357 at the C-terminus of the pore helix. Except for Leu321, the residues that interact with the benzoxadiazole/benzamide core are conserved across SK1-4, consistent with the lack of isoform selectivity for compound 1. The sulfonamide tail of compound 1 extends towards but does not enter the ion pore and the sulfonamide nitrogen hydrogen bonds with Ser318 on S5 (Fig 6D,E). The methoxyphenyl forms an edge-to-face interaction with Phe356 and the methoxy contacts Thr386 on S6, which is one N-terminal helical turn removed from the intracellular gate at Val390 (Fig 6E).

Compared with the ligand-free Ca^{2+}-bound conformation, there are two significant conformational changes in the structure of SK2-4/CaM bound to compound 1. First, there are slight changes in the position of the S5 and pore helix to accommodate the compound 1 core (Fig 6E). These movements translate through Tyr335 and His336 at the extracellular end of S5 to the S3-S4 linker, which is shifted by 1.2 Å in the extracellular direction (Fig 3B, 6E, S6E). In this conformation the hydrophobic constriction at Phe243 would block ion conduction (Fig 6F); however, non-continuous side chain density and a high b-factor (51 $Å^2$ compared to 33 $Å^2$ in the Ca^{2+}-bound state) indicate increased Phe243 flexibility (Fig S4D). Movement of the S3-S4 linker coincides with conformational changes in the selectivity filter similar to those observed with apamin-bound SK2-4 (described above) resulting in a selectivity filter with four K^+ coordination sites (Fig S3D, S4D, S6E,F). This structure further supports the hypothesis that movement of the S3-S4 linker away from the selectivity filter induces a conformation with four K^+ coordination sites.

The second notable conformational change is in the position of the S6 helices. Structural comparisons demonstrate that the methoxy group of compound 1 would clash with Thr386 on S6 in the Ca^{2+}-bound apo conformation of SK2-4 (Fig 6E, S6B). To accommodate the methoxy, Thr386 and the portion of the S6 helices C-terminal to Thr386 shift towards the pore axis akin to the S6 helix shift observed in the Ca^{2+}-free conformation (Fig S6G). Concomitantly, the pore radius at the Val390 intracellular gate is reduced to 1.2 Å demonstrating a clear mechanism for channel inhibition (Fig 6F). Notably, compound 1 closes the gate at Val390 in the presence of saturating Ca^{2+} concentrations demonstrating that this mechanism of inhibition can override the Ca^{2+}-dependent gating. The importance of the methoxy for inhibition was demonstrated by structurally related compounds 2 and 3, in which the benzoxadiazaole of compound 1 is replaced with a benzothiadiazole isostere (Fig S6H,I). Removal of the methoxy from compound 2 produced compound 3 with a 30-fold reduction in potency.

A previous report identified a pair of structurally related compounds that act as selective SK1 inhibitors and activators. This chemical series requires Ser293 on S5 for activity, which corresponds to Leu321 in SK2 suggesting that the SK1 modulators and

compound 1 share the same binding site (Fig S1)[30]. We hypothesized that compound 1 analogs lacking the methoxyphenyl, which our structure and functional data demonstrated is important for SK2 inhibition, may activate SK2. Indeed, a focused screen of compound 1 analogs lacking the methoxyphenyl identified compound 4 as an SK2 activator (Fig 6A, 7A). Like compound 1, compound 4 retains the benzoxadiazole/benzamide core, but the benzamide phenyl features a trifluoromethyl substituent para to the amide. In the 3.1 Å structure of Ca^{2+}-bound SK2-4 in complex with compound 4, clear cryo-EM density demonstrates that the benzoxadiazole/benzamide core occupies the same pocket as observed for compound 1 (Fig 7B, S7, Table 1). However, the S6 helices are in an open conformation and the trifluoromethyl interacts with Ile380, which is 2.5 helical turns N-terminal to Val390, on the S6 helix from a neighboring subunit (Fig 6F, 7B). Structural overlays predict that the trifluoromethyl would clash with Ile380 in the closed conformation of the S6 helices and thereby promote the open conformation to activate SK2 (Fig 7C). Unlike compound 1, compound 4 binding does not induce movement of the S3-S4 linker and the selectivity filter retains a conformation with two K^+ coordination sites (Fig 6F, S7G).

Discussion

The structures of an SK2-4 chimeric channel in the Ca^{2+}-bound and Ca^{2+}-free conformations revealed two unexpected features of the SK2 transmembrane domains. First, the S3-S4 linker forms an anti-parallel β-turn that extends over the S5-S6 segments and interacts with the extracellular pore loops (Fig 3). In this conformation, Phe243 on the S3-S4 linker is positioned directly above the selectivity filter creating a hydrophobic constriction with a radius of 1.8 Å, which prevents the efflux of hydrated K^+ ions (Fig 2D, 3A,C, 4A). Therefore, the Ca^{2+}-bound SK2-4 structure represents a non-conductive conformation even though the intracellular gate is open. Second, the selectivity filter adopts a conformation that resembles non-selective cation channels, such as NaK and HCN, with only two K^+ coordination sites[35,38] (Fig 4A, S4A,B). This selectivity filter conformation seems to be due to the interaction between Asp363 at the C-terminus of the selectivity filter and residues Arg240 and Tyr245 on the S3-S4 linker. In the related SK4 channel the homologous aspartate hydrogen bonds with a pore helix tryptophan[13] (Fig 4C), which is critical for the formation of a selectivity filter with four K^+ coordination sites observed in all K^+ selective channels to date[36,37]. Therefore, by sequestering Asp363 and preventing its interaction with Trp350 in the pore helix, the S3-S4 linker likely induces the two K^+ coordination site selectivity filter observed in the apo SK2-4 structures (Fig 4A, S4A,B). In support of this hypothesis, a similar S3-S4 linker and selectivity filter conformation was observed in the structure of rat SK2, which was published during the preparation of this manuscript, and mutagenesis demonstrated that the interactions between the S3-S4 linker and pore residues induce the observed selectivity filter with two K^+ coordination sites[42]. However, this selectivity filter conformation seems to only exist in a non-conductive state of the channel due to the

extracellular constriction at Phe243 and thus should not affect the K^+ selectivity observed for SK2 and SK2-4 (Fig 1B)[1,31,35-38,40,41].

The subsequent structures of SK2-4 bound to apamin and compound 1 elucidated how the SK channels maintain K^+ selectivity in the conductive state. Conductivity likely requires movement of the S3-S4 linker and Phe243 away from the pore axis to expand the extracellular constriction. Such a shift was observed upon binding of both apamin and compound 1 and was accompanied by four structural rearrangements: 1) Asp363 no longer hydrogen bonds with Arg240 in the S3-S4 linker, 2) Asp363 reorients towards Trp350 in the pore helix, 3) Trp350 rotates to enable a hydrogen bond with Asp363, and 4) Tyr361 in the selectivity filter rotates 180° (Fig 5C,D, S4C,D, S6E,F). These structural changes produce a canonical K^+-selective selectivity filter with four K^+ coordination sites. Based on these structures we predict that in a conductive state of SK2 the extracellular constriction dilates to allow for the flow of K^+ ions. Such a movement would weaken the interactions between the S3-S4 linker and selectivity filter producing a selectivity filter conformation with four K^+ coordination sites to maintain the K^+ selectivity.

The physiological role of S3-S4 linker and the mechanism of extracellular constriction opening require further investigation. One possibility is that in the presence of Ca^{2+} the S3-S4 linker and extracellular constriction exists in an equilibrium between conductive and non-conductive conformations. Such a mechanism may explain some unique properties of SK2 such as its low conductance (~10 pS) and the ability to switch between low- and high-open probability states[1,43]. Indeed, mutation of Phe243 in rat SK2 produced a 2-fold increase in channel conductance[42]. Alternatively, other physiological factors, such as PIP2[45,46], may exist in live cells that modulate the interaction between S3-S4 linker and the selectivity filter. Importantly, the extracellular constriction provides novel opportunities for modulation of SK2.

The structures and functional experiments presented here revealed two binding sites for SK2 modulators and identified three distinct mechanisms of modulation. The bee toxin apamin binds at the extracellular opening of the pore, at the same site as UCL1684, to a site co-formed by the S3-S4 linker from each subunit, explaining why both the S3-S4 linker and pore residues were found to be important for apamin binding and inhibition (Fig 5)[18-20,42]. The two essential arginine residues (13 and 14) of apamin are directed towards the selectivity filter and form cation-π interactions with the essential S3-S4 linker residue Phe243, blocking K^+ ion efflux and inhibiting conduction. In support of this binding interaction and mechanism of inhibition, a Phe243Ala mutant abolishes apamin inhibition (Fig 5B). The elucidated apamin binding site and mechanism of inhibition may enable development of new modulators that target the extracellular domains of SK2.

A second partially cryptic binding pocket at the interface of the S5, pore helix, and S6 was revealed through the identification and characterization of compounds 1 and 4 (Fig 6D, 7B). This binding pocket interacts with a benzoxadiazole/benzamide core and the

functional arm on the benzamide phenyl interacts with the S6 helices to modulate SK2 activity. For compound 1, a sulfonamide methoxyphenyl meta to the amide contacts Thr386 on the S6 helix in the same subunit to induce the closed conformation of the S6 helices and inhibit the channel (Fig 6D,E,F). Conversely, for compound 4 the trifluoromethyl para to the amide contacts Ile380 on the S6 helix from a neighboring subunit to promote the open conformation of the S6 helices and activate the channel (Fig 6F, 7B,C). Further optimization of the functional groups on the benzamide phenyl that interact with S6 helices may produce more potent activators and/or inhibitors. For example, more potent activation may be achieved if the interaction between compound 4 and the neighboring S6 was closer to the intracellular gate at Val390 (i.e., within 1 helical turn). Producing isoform selective modulators targeting the compound 1/4 binding pocket may prove more challenging due to the high sequence conservation of residues lining the pocket. However, SK1 modulators that are predicted to share the same binding site as compound 1 take advantage of a unique S5 Ser to confer selectivity over SK2 and SK3 suggesting isoform selectivity could be achieved through further optimization[30].

In summary, this study characterized SK2 channel dynamics as well as mechanisms of pharmacological modulation utilizing a SK2-4 chimera, containing the S1-S6 transmembrane regions of human SK2 and the intracellular domains of human SK4. SK2-4 is K^+-selective, activated by Ca^{2+}, sensitive to SK2 modulators that bind the S1-S6 transmembrane regions, and suitable for cryo-EM structure determination. The findings revealed critical structural features and mechanisms of SK2 channel modulation, providing a framework for development of targeted therapeutics for the SK channel family.

Author Contributions

S.J.C, S.K., W.L., and J.R.W. conceived the project and designed the experiments. Cryo-EM data was collected by M.K. and processed by S.J.C, M.K., and J.R.W. Structural analysis was completed by S.J.C., W.A.W, and J.R.W. Electrophysiological characterization of SK2-4, SK2 mutant characterization, HTS screening, characterization of compounds 1-4 completed by W.L., Y.T.L., J.H., W.G. Characterization and optimization of compound 1 and compound 4 completed by S.K. and S.P. The manuscript was written by S.J.C, W.L., S.K., and J.R.W. with inputs from all authors.

Declaration of interests

All authors are employees of Novartis.

References

1. Kohler, M., Hirschberg, B., Bond, C.T., Kinzie, J.M., Marrion, N.V., Maylie, J., and Adelman, J.P. (1996). Small-conductance, calcium-activated potassium channels from mammalian brain. Science *273*, 1709-1714. 10.1126/science.273.5282.1709.
2. Bond, C.T., Herson, P.S., Strassmaier, T., Hammond, R., Stackman, R., Maylie, J., and Adelman, J.P. (2004). Small conductance Ca2+-activated K+ channel knock-out mice reveal the identity of calcium-dependent afterhyperpolarization currents. J Neurosci *24*, 5301-5306. 10.1523/JNEUROSCI.0182-04.2004.
3. Blatz, A.L., and Magleby, K.L. (1986). Single apamin-blocked Ca-activated K+ channels of small conductance in cultured rat skeletal muscle. Nature *323*, 718-720. 10.1038/323718a0.
4. Adelman, J.P., Maylie, J., and Sah, P. (2012). Small-conductance Ca2+-activated K+ channels: form and function. Annu Rev Physiol *74*, 245-269. 10.1146/annurev-physiol-020911-153336.
5. Hammond, R.S., Bond, C.T., Strassmaier, T., Ngo-Anh, T.J., Adelman, J.P., Maylie, J., and Stackman, R.W. (2006). Small-conductance Ca2+-activated K+ channel type 2 (SK2) modulates hippocampal learning, memory, and synaptic plasticity. J Neurosci *26*, 1844-1853. 10.1523/JNEUROSCI.4106-05.2006.
6. Zhang, Q., Timofeyev, V., Lu, L., Li, N., Singapuri, A., Long, M.K., Bond, C.T., Adelman, J.P., and Chiamvimonvat, N. (2008). Functional roles of a Ca2+-activated K+ channel in atrioventricular nodes. Circ Res *102*, 465-471. 10.1161/CIRCRESAHA.107.161778.
7. Hopf, F.W., Simms, J.A., Chang, S.J., Seif, T., Bartlett, S.E., and Bonci, A. (2011). Chlorzoxazone, an SK-type potassium channel activator used in humans, reduces excessive alcohol intake in rats. Biol Psychiatry *69*, 618-624. 10.1016/j.biopsych.2010.11.011.
8. Alvina, K., and Khodakhah, K. (2010). KCa channels as therapeutic targets in episodic ataxia type-2. J Neurosci *30*, 7249-7257. 10.1523/JNEUROSCI.6341-09.2010.
9. Anderson, N.J., Slough, S., and Watson, W.P. (2006). In vivo characterisation of the small-conductance KCa (SK) channel activator 1-ethyl-2-benzimidazolinone (1-EBIO) as a potential anticonvulsant. Eur J Pharmacol *546*, 48-53. 10.1016/j.ejphar.2006.07.007.
10. Allen, D., Nakayama, S., Kuroiwa, M., Nakano, T., Palmateer, J., Kosaka, Y., Ballesteros, C., Watanabe, M., Bond, C.T., Lujan, R., et al. (2011). SK2 channels are neuroprotective for ischemia-induced neuronal cell death. J Cereb Blood Flow Metab *31*, 2302-2312. 10.1038/jcbfm.2011.90.
11. Proulx, E., Fraser, P., McLaurin, J., and Lambe, E.K. (2015). Impaired Cholinergic Excitation of Prefrontal Attention Circuitry in the TgCRND8 Model of Alzheimer's Disease. J Neurosci *35*, 12779-12791. 10.1523/JNEUROSCI.4501-14.2015.
12. Diness, J.G., Skibsbye, L., Jespersen, T., Bartels, E.D., Sorensen, U.S., Hansen, R.S., and Grunnet, M. (2011). Effects on atrial fibrillation in aged hypertensive rats by Ca(2+)-activated K(+) channel inhibition. Hypertension *57*, 1129-1135. 10.1161/HYPERTENSIONAHA.111.170613.

13. Lee, C.-H., and Mackinnon, R. (2018). Activation mechanism of a human SK-calmodulin channel complex elucidated by cryo-EM structures. Science *360*, 508-513. 10.1126/science.aas9466.
14. Doyle, D.A., Morais Cabral, J., Pfuetzner, R.A., Kuo, A., Gulbis, J.M., Cohen, S.L., Chait, B.T., and MacKinnon, R. (1998). The structure of the potassium channel: molecular basis of K+ conduction and selectivity. Science *280*, 69-77. 10.1126/science.280.5360.69.
15. Xia, X.M., Fakler, B., Rivard, A., Wayman, G., Johnson-Pais, T., Keen, J.E., Ishii, T., Hirschberg, B., Bond, C.T., Lutsenko, S., et al. (1998). Mechanism of calcium gating in small-conductance calcium-activated potassium channels. Nature *395*, 503-507. 10.1038/26758.
16. Brown, B.M., Shim, H., Christophersen, P., and Wulff, H. (2020). Pharmacology of Small- and Intermediate-Conductance Calcium-Activated Potassium Channels. Annu Rev Pharmacol Toxicol *60*, 219-240. 10.1146/annurev-pharmtox-010919-023420.
17. Shim, H., Brown, B.M., Singh, L., Singh, V., Fettinger, J.C., Yarov-Yarovoy, V., and Wulff, H. (2019). The Trials and Tribulations of Structure Assisted Design of K(Ca) Channel Activators. Front Pharmacol *10*, 972. 10.3389/fphar.2019.00972.
18. Nolting, A., Ferraro, T., D'Hoedt, D., and Stocker, M. (2007). An amino acid outside the pore region influences apamin sensitivity in small conductance Ca2+-activated K+ channels. J Biol Chem *282*, 3478-3486. 10.1074/jbc.M607213200.
19. Weatherall, K.L., Seutin, V., Liegeois, J.F., and Marrion, N.V. (2011). Crucial role of a shared extracellular loop in apamin sensitivity and maintenance of pore shape of small-conductance calcium-activated potassium (SK) channels. Proc Natl Acad Sci U S A *108*, 18494-18499. 10.1073/pnas.1110724108.
20. Lamy, C., Goodchild, S.J., Weatherall, K.L., Jane, D.E., Liegeois, J.F., Seutin, V., and Marrion, N.V. (2010). Allosteric block of KCa2 channels by apamin. J Biol Chem *285*, 27067-27077. 10.1074/jbc.M110.110072.
21. Messier, C., Mourre, C., Bontempi, B., Sif, J., Lazdunski, M., and Destrade, C. (1991). Effect of apamin, a toxin that inhibits Ca(2+)-dependent K+ channels, on learning and memory processes. Brain Res *551*, 322-326. 10.1016/0006-8993(91)90950-z.
22. Kuzmenkov, A.I., Peigneur, S., Nasburg, J.A., Mineev, K.S., Nikolaev, M.V., Pinheiro-Junior, E.L., Arseniev, A.S., Wulff, H., Tytgat, J., and Vassilevski, A.A. (2022). Apamin structure and pharmacology revisited. Front Pharmacol *13*, 977440. 10.3389/fphar.2022.977440.
23. Vincent, J.P., Schweitz, H., and Lazdunski, M. (1975). Structure-function relationships and site of action of apamin, a neurotoxic polypeptide of bee venom with an action on the central nervous system. Biochemistry *14*, 2521-2525. 10.1021/bi00682a035.
24. Ishii, T.M., Maylie, J., and Adelman, J.P. (1997). Determinants of apamin and d-tubocurarine block in SK potassium channels. J Biol Chem *272*, 23195-23200. 10.1074/jbc.272.37.23195.
25. Castle, N.A., Haylett, D.G., Morgan, J.M., and Jenkinson, D.H. (1993). Dequalinium: a potent inhibitor of apamin-sensitive K+ channels in hepatocytes and of nicotinic responses in skeletal muscle. Eur J Pharmacol *236*, 201-207. 10.1016/0014-2999(93)90590-e.

26. Chen, J.Q., Galanakis, D., Ganellin, C.R., Dunn, P.M., and Jenkinson, D.H. (2000). bis-Quinolinium cyclophanes: 8,14-diaza-1,7(1, 4)-diquinolinacyclotetradecaphane (UCL 1848), a highly potent and selective, nonpeptidic blocker of the apamin-sensitive Ca(2+)-activated K(+) channel. J Med Chem *43*, 3478-3481. 10.1021/jm000904v.
27. Jenkins, D.P., Strobaek, D., Hougaard, C., Jensen, M.L., Hummel, R., Sorensen, U.S., Christophersen, P., and Wulff, H. (2011). Negative gating modulation by (R)-N-(benzimidazol-2-yl)-1,2,3,4-tetrahydro-1-naphthylamine (NS8593) depends on residues in the inner pore vestibule: pharmacological evidence of deep-pore gating of K(Ca)2 channels. Mol Pharmacol *79*, 899-909. 10.1124/mol.110.069807.
28. Simo-Vicens, R., Kirchhoff, J.E., Dolce, B., Abildgaard, L., Speerschneider, T., Sorensen, U.S., Grunnet, M., Diness, J.G., and Bentzen, B.H. (2017). A new negative allosteric modulator, AP14145, for the study of small conductance calcium-activated potassium (K(Ca) 2) channels. Br J Pharmacol *174*, 4396-4408. 10.1111/bph.14043.
29. Saljic, A., Heijman, J., and Dobrev, D. (2024). From Atrial Small-conductance Calcium-activated Potassium Channels to New Antiarrhythmics. Eur Cardiol *19*, e26. 10.15420/ecr.2024.41.
30. Hougaard, C., Hammami, S., Eriksen, B.L., Sørensen, U.S., Jensen, M.L., Strøbæk, D., and Christophersen, P. (2012). Evidence for a Common Pharmacological Interaction Site on K_{Ca}2 Channels Providing Both Selective Activation and Selective Inhibition of the Human K_{Ca}2.1 Subtype. Molecular Pharmacology *81*, 210-219. 10.1124/mol.111.074252.
31. Desai, R., Peretz, A., Idelson, H., Lazarovici, P., and Attali, B. (2000). Ca2+-activated K+ channels in human leukemic Jurkat T cells. Molecular cloning, biochemical and functional characterization. J Biol Chem *275*, 39954-39963. 10.1074/jbc.M001562200.
32. Zhou, Y., Morais-Cabral, J.H., Kaufman, A., and MacKinnon, R. (2001). Chemistry of ion coordination and hydration revealed by a K+ channel-Fab complex at 2.0 A resolution. Nature *414*, 43-48. 10.1038/35102009.
33. Morais-Cabral, J.H., Zhou, Y., and MacKinnon, R. (2001). Energetic optimization of ion conduction rate by the K+ selectivity filter. Nature *414*, 37-42. 10.1038/35102000.
34. Lockless, S.W. (2015). Determinants of cation transport selectivity: Equilibrium binding and transport kinetics. J Gen Physiol *146*, 3-13. 10.1085/jgp.201511371.
35. Shi, N., Ye, S., Alam, A., Chen, L., and Jiang, Y. (2006). Atomic structure of a Na+- and K+-conducting channel. Nature *440*, 570-574. 10.1038/nature04508.
36. Derebe, M.G., Sauer, D.B., Zeng, W., Alam, A., Shi, N., and Jiang, Y. (2011). Tuning the ion selectivity of tetrameric cation channels by changing the number of ion binding sites. Proc Natl Acad Sci U S A *108*, 598-602. 10.1073/pnas.1013636108.
37. Sauer, D.B., Zeng, W., Raghunathan, S., and Jiang, Y. (2011). Protein interactions central to stabilizing the K+ channel selectivity filter in a four-sited configuration for selective K+ permeation. Proc Natl Acad Sci U S A *108*, 16634-16639. 10.1073/pnas.1111688108.
38. Lee, C.-H., and Mackinnon, R. (2017). Structures of the Human HCN1 Hyperpolarization-Activated Channel. Cell *168*, 111-120.e111. 10.1016/j.cell.2016.12.023.

39. Shin, N., Soh, H., Chang, S., Kim, D.H., and Park, C.-S. (2005). Sodium Permeability of a Cloned Small-Conductance Calcium-Activated Potassium Channel. Biophysical Journal *89*, 3111-3119. 10.1529/biophysj.105.069542.
40. Park, Y.B. (1994). Ion selectivity and gating of small conductance Ca(2+)-activated K+ channels in cultured rat adrenal chromaffin cells. J Physiol *481 (Pt 3)*, 555-570. 10.1113/jphysiol.1994.sp020463.
41. Jager, H., Adelman, J.P., and Grissmer, S. (2000). SK2 encodes the apamin-sensitive Ca(2+)-activated K(+) channels in the human leukemic T cell line, Jurkat. FEBS Lett *469*, 196-202. 10.1016/s0014-5793(00)01236-9.
42. Nam, Y.W., Im, D., Garcia, A.S.C., Tringides, M.L., Nguyen, H.M., Liu, Y., Orfali, R., Ramanishka, A., Pintilie, G., Su, C.C., et al. (2025). Cryo-EM structures of the small-conductance Ca(2+)-activated K(Ca)2.2 channel. Nat Commun *16*, 3690. 10.1038/s41467-025-59061-1.
43. Hirschberg, B., Maylie, J., Adelman, J.P., and Marrion, N.V. (1998). Gating of recombinant small-conductance Ca-activated K+ channels by calcium. J Gen Physiol *111*, 565-581. 10.1085/jgp.111.4.565.
44. Ishii, T.M., Silvia, C., Hirschberg, B., Bond, C.T., Adelman, J.P., and Maylie, J. (1997). A human intermediate conductance calcium-activated potassium channel. Proc Natl Acad Sci U S A *94*, 11651-11656. 10.1073/pnas.94.21.11651.
45. Woltz, R.L., Zheng, Y., Choi, W., Ngo, K., Trinh, P., Ren, L., Thai, P.N., Harris, B.J., Han, Y., Rouen, K.C., et al. (2024). Atomistic mechanisms of the regulation of small-conductance Ca(2+)-activated K(+) channel (SK2) by PIP2. Proc Natl Acad Sci U S A *121*, e2318900121. 10.1073/pnas.2318900121.
46. Zhang, M., Meng, X.Y., Cui, M., Pascal, J.M., Logothetis, D.E., and Zhang, J.F. (2014). Selective phosphorylation modulates the PIP2 sensitivity of the CaM-SK channel complex. Nat Chem Biol *10*, 753-759. 10.1038/nchembio.1592.
47. Zheng, S.Q., Palovcak, E., Armache, J.P., Verba, K.A., Cheng, Y., and Agard, D.A. (2017). MotionCor2: anisotropic correction of beam-induced motion for improved cryo-electron microscopy. Nat Methods *14*, 331-332. 10.1038/nmeth.4193.
48. Punjani, A., Rubinstein, J.L., Fleet, D.J., and Brubaker, M.A. (2017). cryoSPARC: algorithms for rapid unsupervised cryo-EM structure determination. Nat Methods *14*, 290-296. 10.1038/nmeth.4169.
49. Punjani, A., Zhang, H., and Fleet, D.J. (2020). Non-uniform refinement: adaptive regularization improves single-particle cryo-EM reconstruction. Nat Methods *17*, 1214-1221. 10.1038/s41592-020-00990-8.
50. Grant, T., Rohou, A., and Grigorieff, N. (2018). cisTEM, user-friendly software for single-particle image processing. Elife *7*. 10.7554/eLife.35383.
51. Emsley, P., Lohkamp, B., Scott, W.G., and Cowtan, K. (2010). Features and development of Coot. Acta Crystallogr D Biol Crystallogr *66*, 486-501. 10.1107/S0907444910007493.
52. Pettersen, E.F., Goddard, T.D., Huang, C.C., Couch, G.S., Greenblatt, D.M., Meng, E.C., and Ferrin, T.E. (2004). UCSF Chimera--a visualization system for exploratory research and analysis. J Comput Chem *25*, 1605-1612. 10.1002/jcc.20084.
53. Afonine, P.V., Poon, B.K., Read, R.J., Sobolev, O.V., Terwilliger, T.C., Urzhumtsev, A., and Adams, P.D. (2018). Real-space refinement in PHENIX for cryo-EM and

crystallography. Acta Crystallogr D Struct Biol *74*, 531-544. 10.1107/S2059798318006551.

54. Chen, V.B., Arendall, W.B., 3rd, Headd, J.J., Keedy, D.A., Immormino, R.M., Kapral, G.J., Murray, L.W., Richardson, J.S., and Richardson, D.C. (2010). MolProbity: all-atom structure validation for macromolecular crystallography. Acta Crystallogr D Biol Crystallogr *66*, 12-21. 10.1107/S0907444909042073.

Figures

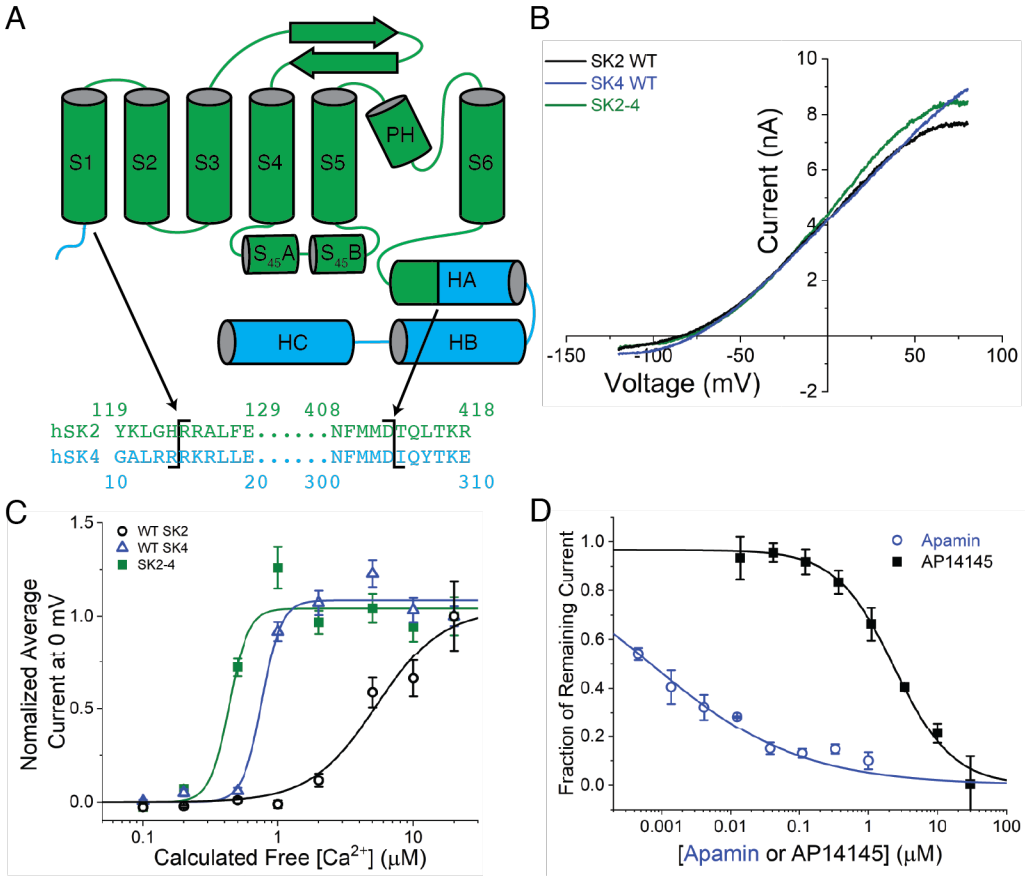

Figure 1 Design and characterization of SK2-4 chimera. A) Cartoon representation of the SK2-4 chimera. Residue numbers in the SK2 regions of the structure correspond to the human SK2 sequence described by Desai *et al*.[31] and the SK4 regions of the structure are numbered sequentially from the SK2 regions. The sequence alignment of human SK2 (green) and human SK4 (cyan) indicate the chimera boundaries (black lines). B) Representative current traces in response to a ramp voltage protocol from -120 mV to 80 mV show that reversal potentials of WT SK2 (black), SK4 (blue), and SK2-4 (green) currents are all around -85 mV demonstrating similar potassium selectivity. Shown SK current traces are isolated by subtracting leak current under saturating concentration of inhibitors (UCL1684 or TRAM-34). C) SK2-4 (green squares) is activated by increasing intracellular Ca^{2+} like WT SK2 (black circles) and SK4 channels (blue triangles). Current amplitudes were normalized to average value at 20 μM Ca^{2+}. Apparent EC_{50}s for SK2, SK4 and SK2-4 are 5.4 μM, 0.8 μM and 0.4 μM, respectively. Note that actual intracellular free [Ca^{2+}] might differ from intracellular buffer due to limit of diffusion in whole-cell configuration. Data points reflect mean +/- SEM (n=4) D) SK2-4 is inhibited by apamin (blue circles, IC_{50}=0.7 nM), which targets the extracellular domains of SK2, and AP14145 (black squares, IC_{50}=2.4 μM), which targets the transmembrane domains of SK2. Data points reflect mean +/- SD (n=4).

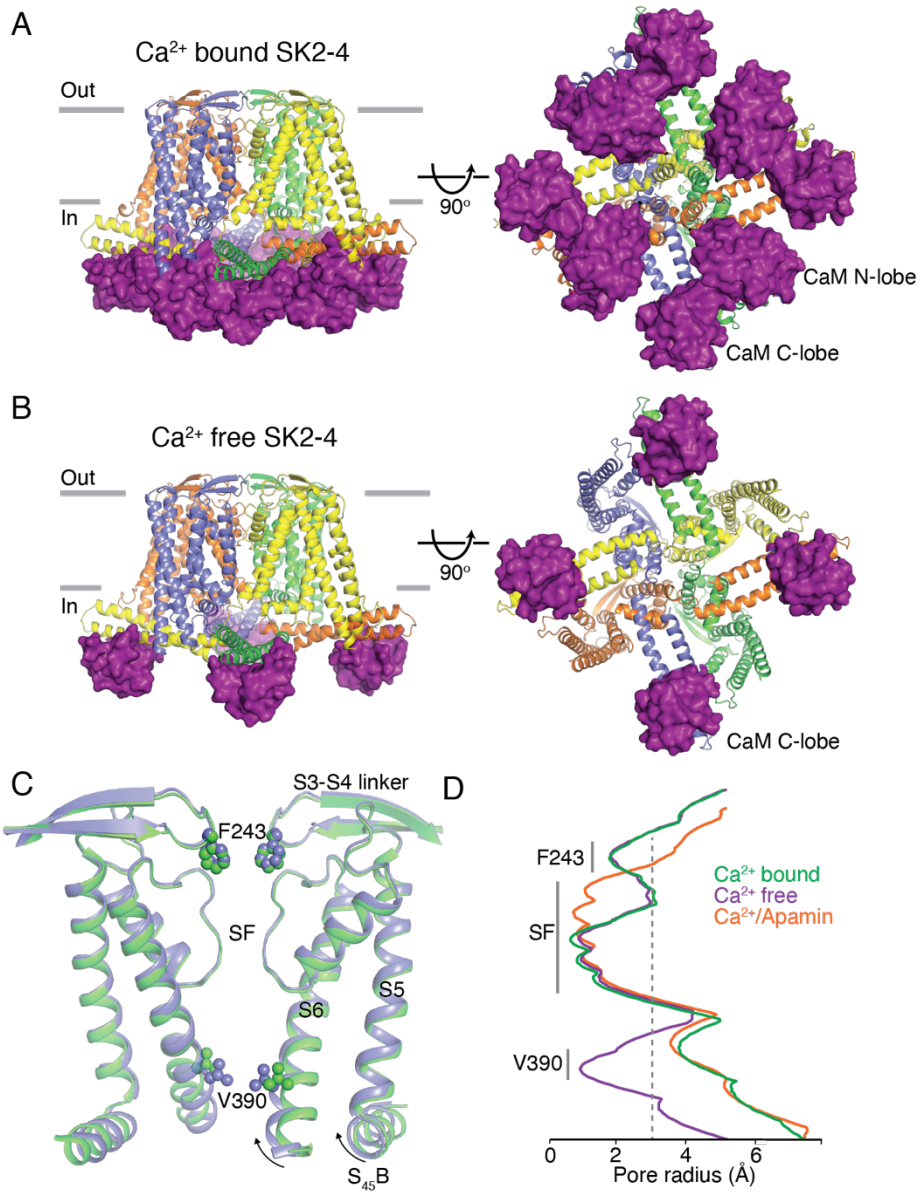

Figure 2 SK2-4 chimera architecture. Structures of Ca^{2+}-bound (A) and Ca^{2+}-free (B) SK2-4. SK2-4 is shown as a cartoon with each subunit of the tetramer a different color. The grey lines (left) indicate membrane boundaries. In Ca^{2+}-bound SK2-4 (A) both the N- and C-lobes of CaM (purple surface) are associated with the intracellular domains. In Ca^{2+}-free SK2-4 (B) only the CaM C-lobe is bound (purple surface) and the N-lobe is dissociated (not shown). C) Overlay of the K^+ pore from Ca^{2+}-bound (green) and Ca^{2+}-free (lavender) SK2-4 structures. Same view as left panels of (A) and (B) but only 2 subunits are shown. D) Pore radii of Ca^{2+}-bound (green), Ca^{2+}-free (lavender), and apamin-bound (orange) SK2-4. The location of the intracellular gate (Val390), selectivity filter (SF), and extracellular constriction (Phe243) are indicated. Grey dashed line indicates the radius of hydrated K^+ (3 Å).

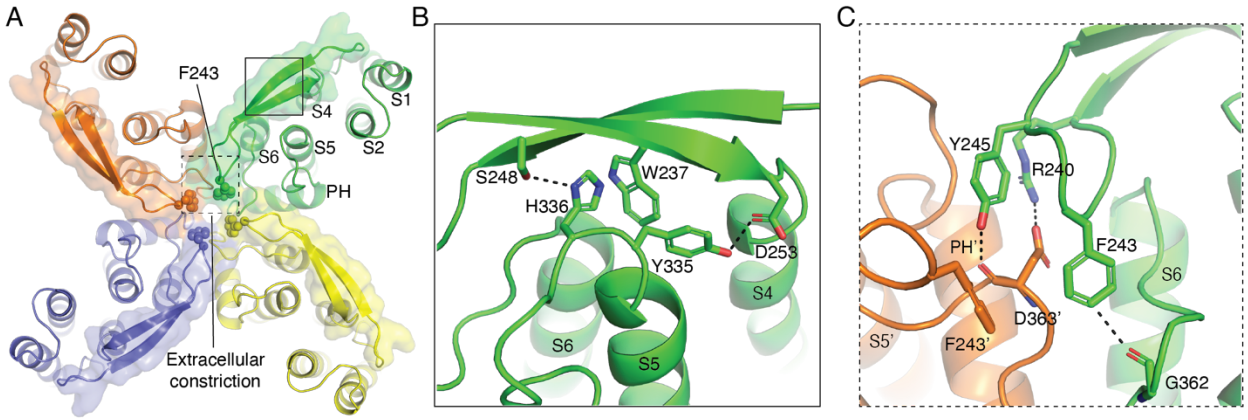

Figure 3 S3-S4 loop architecture. A) Extracellular view of Ca^{2+}-bound SK2-4 with each subunit of the tetramer a different color. The S3-S4 linker (surface and cartoon) extends over the S5 and S6 helices. Phe243 residues (spheres) form an extracellular constriction with a radius of 1.8 Å. Boxes indicate location of the interactions shown in (B) and (C). B) Interactions between the S3-S4 linker and the C-terminus of S5. His336 forms an edge-to-face interaction with Trp237 and hydrogen bond with Ser248 (dashed lines). Tyr335 forms a hydrogen bond with D253 (dashed lines). C) Interactions between the S3-S4 linker and the C-terminus of the selectivity filter. Arg240 and Tyr245 (green sticks) from the S3-S4 linker form a salt bridge and hydrogen bond (dashed lines) with side chain and backbone carbonyl of Asp363 from the neighboring subunit (orange sticks), respectively. Phe243 (green sticks) forms an edge-to-face interaction with the neighboring Phe243 (orange sticks) and is in position to form a C-H/O interaction (dashed line) with Gly262 (green sticks) from the same subunit.

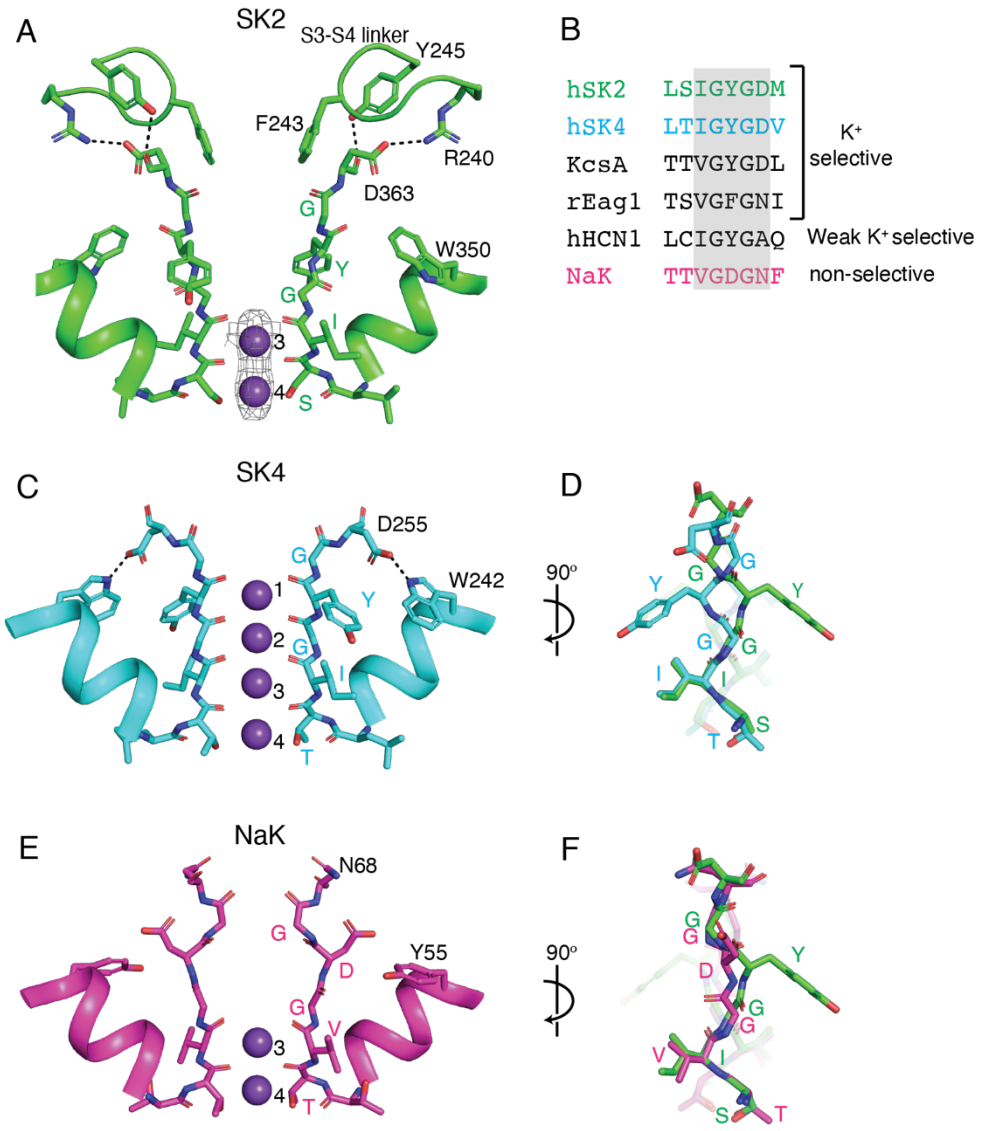

Figure 4 Selectivity filter conformation of SK2-4. A) Ca^{2+}-bound SK2-4 selectivity filter structure (green). Arg240 and Tyr245 from the S3-S4 form a salt bridge and hydrogen bond (dashed lines) with Asp363 and the selectivity filter adopts a conformation with two K^+ coordination sites (purple spheres, density shown). B) Sequence alignment of selectivity filter from K^+ selective channels (hSK2, hSK4, KcsA, hEag) and non-selective cation channels (hHCN and NaK) C) Structure of hSK4 selectivity filter (cyan, PDB: 6CNN). In SK4 there is a conserved hydrogen bond between the selectivity filter Asp255 and pore helix Trp242 (dashed lines) and the selectivity filter conformation creates four occupied K^+ coordination sites (purple spheres). D) Overlay of the SK2-4 (green) and the SK4 (cyan) selectivity filter with a 90° rotation from (C). E) Structure of NaK selectivity filter (magenta, PDB: 2AHZ). In NaK there is no interaction between the selectivity filter Asn68 and the pore helix Tyr55 and

the selectivity filter adopts a conformation with two occupied K^+ coordination sites (purple spheres). F) Overlay of the SK2-4 (green) and the NaK (magenta) selectivity filter with a 90° rotation from (E).

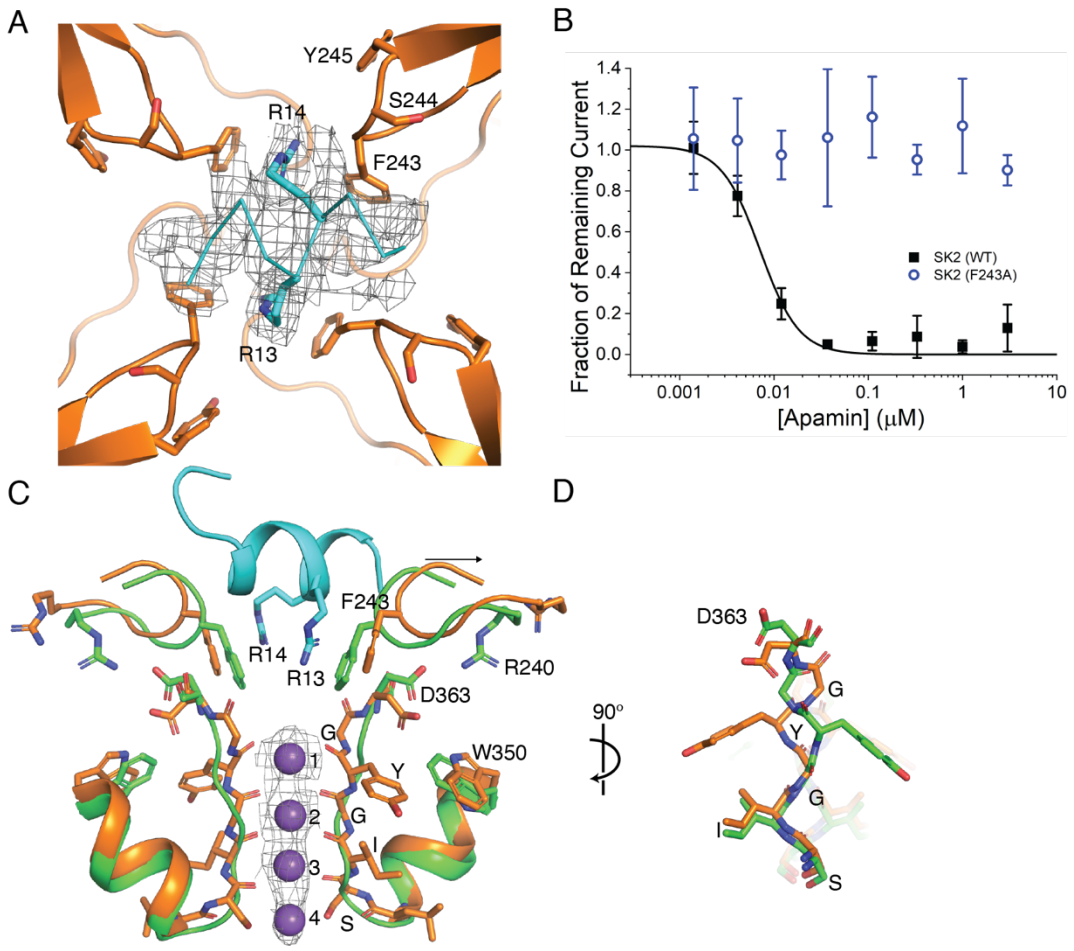

Figure 5 Mechanism of apamin inhibition. A) Extracellular view of apamin binding site. Apamin (cyan ribbon, density shown) binds to the S3-S4 extracellular gate. Apamin Arg13 and Arg14 (cyan sticks) and S3-S4 linker residues (orange) that surround the apamin binding site are shown as sticks. B) Apamin sensitivity of WT SK2 (black squares) and SK2 F243A (blue circles). Data points represent mean +/- SD (n=6). The F243A mutant is insensitive to apamin up to 3 μM. C) Overlay of Ca^{2+}-bound SK2-4 selectivity filter (green cartoon) and apamin-bound SK2-4 selectivity filter (orange, selectivity filter shown as sticks and S3-S4 linker and pore helix shown as a cartoon). Upon apamin (cyan cartoon) binding the S3-S4 linker retracts from the pore axis (black arrow) and the selectivity filter adopts a conformation with four K^+ coordination sites (purple spheres, density shown). D) 90° degree rotation of (C).

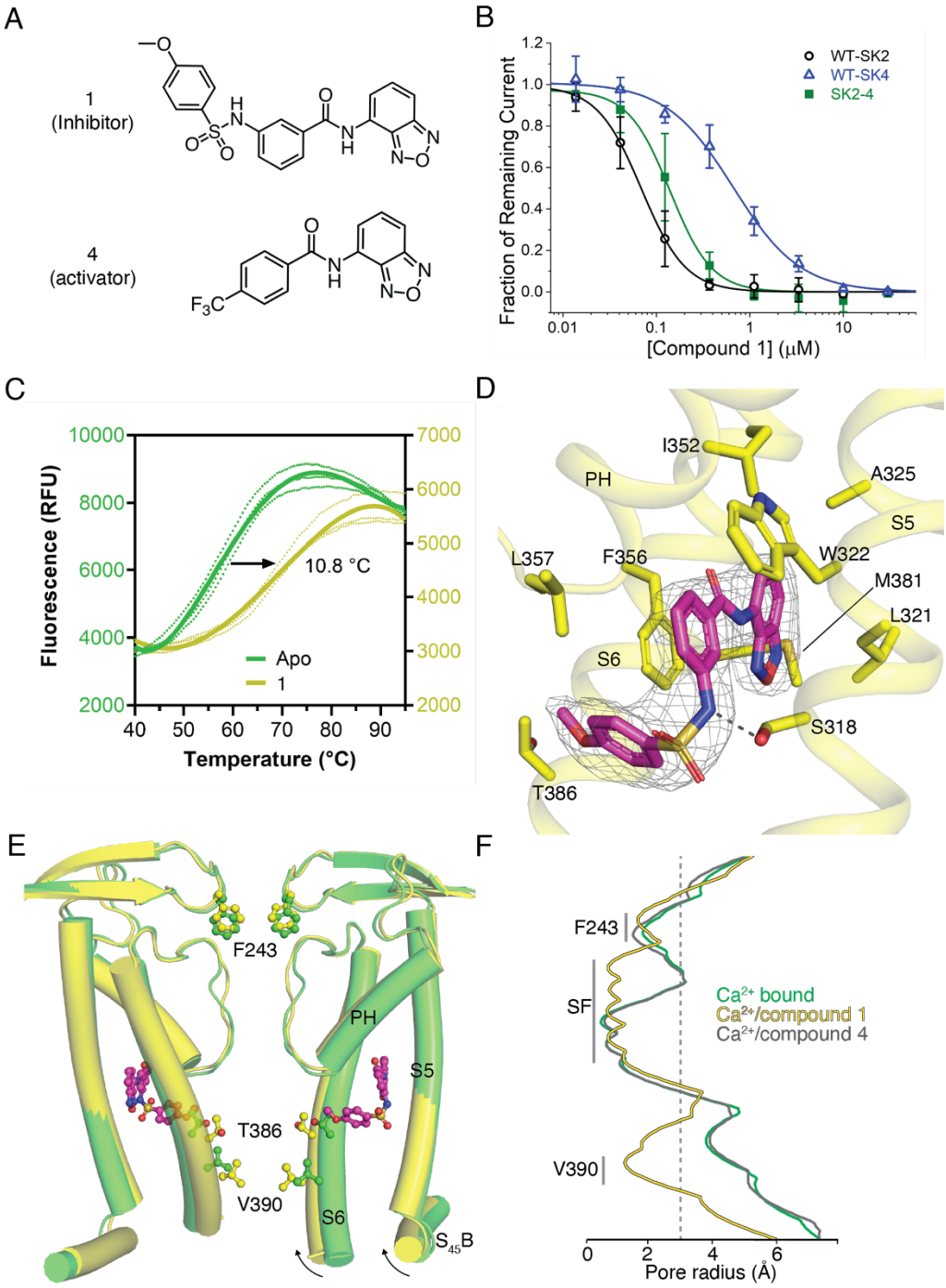

Figure 6 Mechanism of compound 1 inhibition. A) Structure of compound 1 (inhibitor) and compound 4 (activator). B) Potency of compound 1 on SK2 (black circles, IC_{50}=69 nM), SK2-4 (green squares, IC_{50}=140 nM), and SK4 (blue triangles, IC_{50}=0.66 μM). Data points represent mean +/- SD (n=4). C) Melting curves of Ca^{2+}-bound SK2-4 in the absence (green, T_m = 58.7 °C) and presence (yellow, T_m = 69.5 °C) of compound 1 measured by CPM indicates target engagement. D) Compound 1 (magenta sticks, density shown) interacts with a pocket formed by the S5, pore helix, and S6. Ser318 of S5 is in position to hydrogen bond (dashed line) with the sulfonamide nitrogen of

compound 1. E) Overlay of the K^+ pore of Ca^{2+}-bound SK2-4 (green) and compound 1-bound SK2-4 (yellow) (only 2 subunits are shown for clarity). The methoxy of compound 1 (magenta spheres) clashes with S6 Thr386 (spheres) and induces a movement of the S6 and $S_{45}B$ helices toward the pore axis (arrow) to close the intracellular gate (Val390, spheres). D) Pore radii of Ca^{2+}-bound (green), compound 1-bound (yellow), and compound 4-bound (grey) SK2-4. The location of the intracellular gate (Val390), selectivity filter (SF), and extracellular constriction (Phe243) are indicated. Grey dashed line indicates the radius of hydrated K^+ (3 Å).

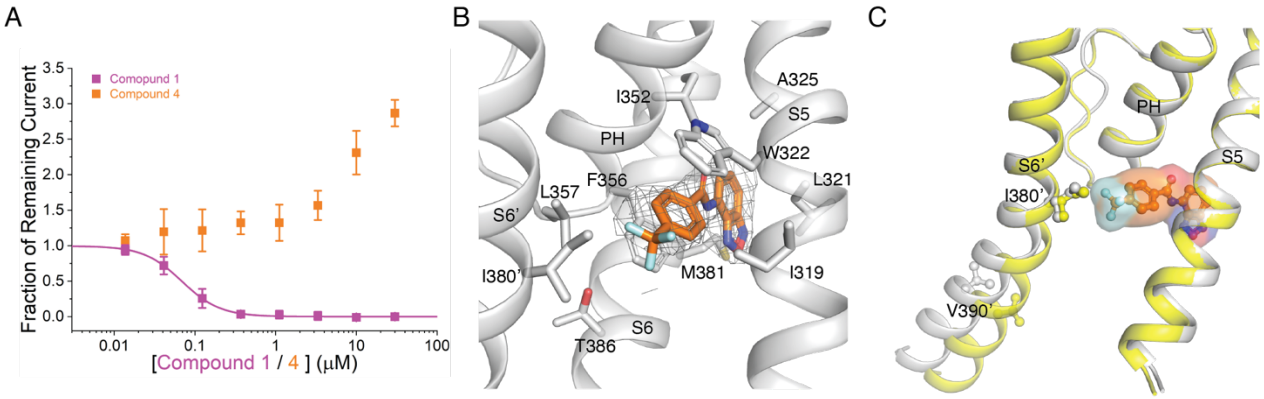

Figure 7 Mechanism of compound 4 activation. A) Comparison of activation and inhibition curves for compound 4 (orange squares) and compound 1 (magenta squares), respectively. Data points represent mean +/- SD (n=6). B) Compound 4 (orange sticks, density shown) interacts with a pocket formed by the S5, pore helix, and S6 and the trifluoromethyl extends towards Ile380 on the neighboring S6 (S6'). C) Overlay of compound 1-bound SK2-4 (yellow) and compound 4-bound (grey) SK2-4. In the closed state of the S6 helices (yellow cartoon) the trifluoromethyl of compound 4 clashes with Ile380 (yellow sticks) on the S6 helix (S6') of the neighboring subunit (2.3 Å distance). In the open state of the S6 helices (grey cartoon), Ile380 (grey sticks) is 3.1 Å distant the trifluoromethyl minimizing this clash.

Supplementary Figures

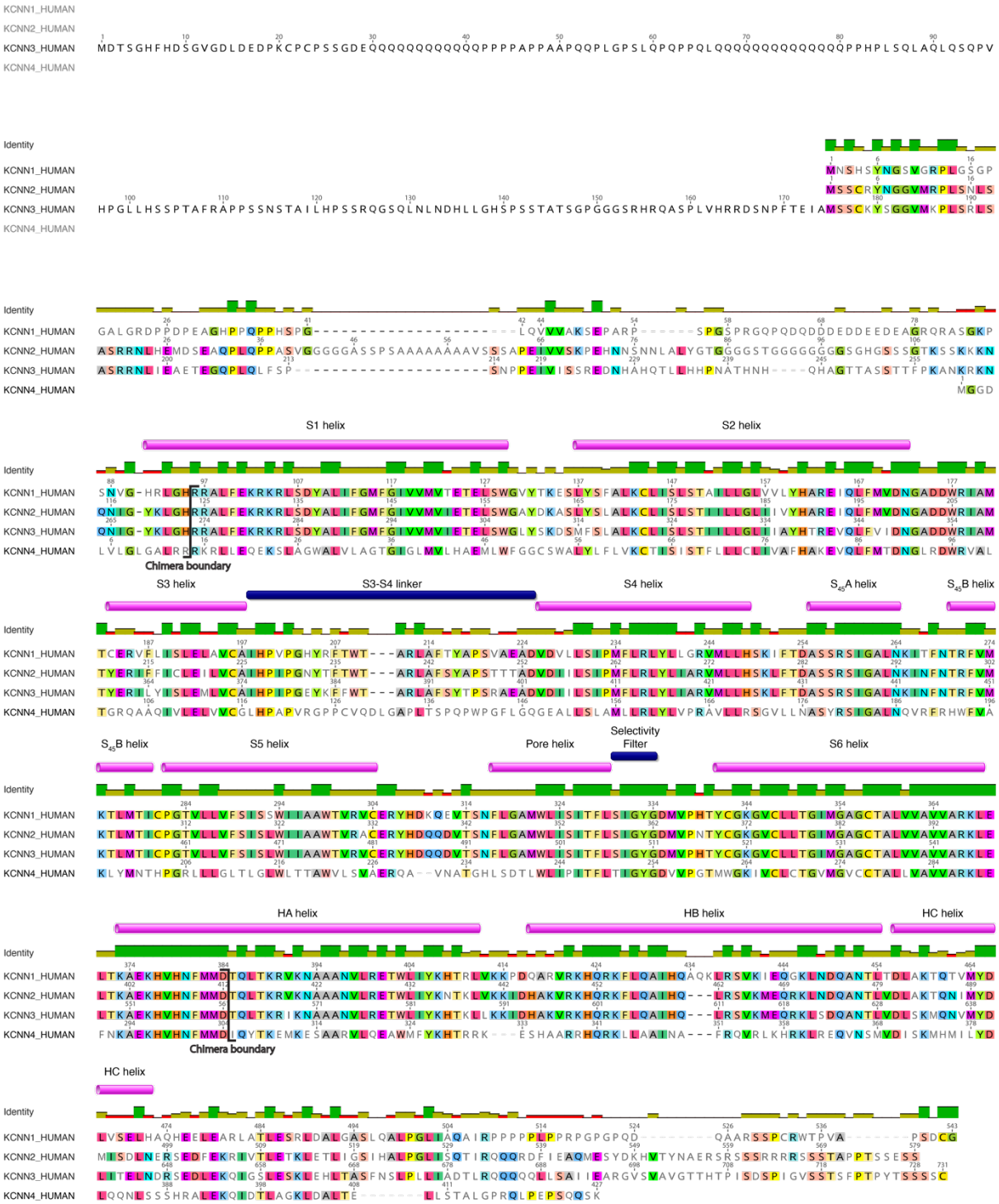

Figure S1 Sequence alignment of human SK1, SK2, SK3, and SK4. SK2 structural features and chimera boundaries are annotated. Sequence identity is shown in the graph above the sequences.

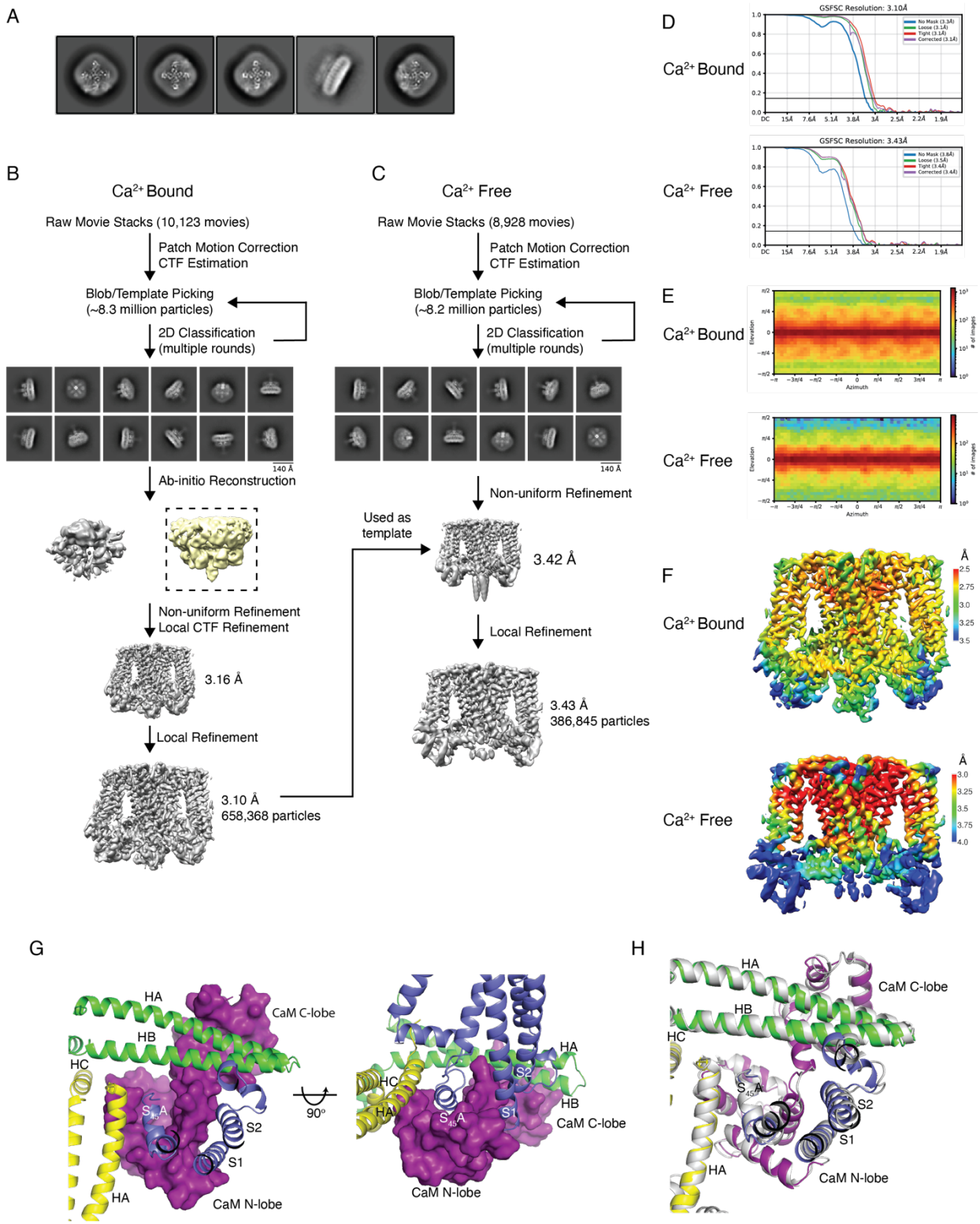

Figure S2 Structure determination of Ca^{2+}-bound SK2-4 and Ca^{2+}-free SK2-4. A) 2D class averages of WT SK2 showing disorder in the intracellular region. Cryo-EM structure determination flowchart for (B) Ca^{2+}-bound SK2-4 and (C) Ca^{2+}-free SK2-4. (D) FSC curves, (E) angular distribution, and (F) local resolution estimates for Ca^{2+}-bound

SK2-4 and Ca^{2+}-free SK2-4. G) Interactions between the SK2-4 intracellular domains and CaM (surface, purple) in the Ca^{2+}-bound conformation of SK2-4 (cartoon, each subunit has a different color). The CaM C-lobe interacts with the HA and HB helices and the N-lobe interacts with the $S_{45}A$. H) Overlay of the intracellular domains from SK2-4 (colored as in G) and SK4 (grey) demonstrate a similar CaM binding interaction in each structure.

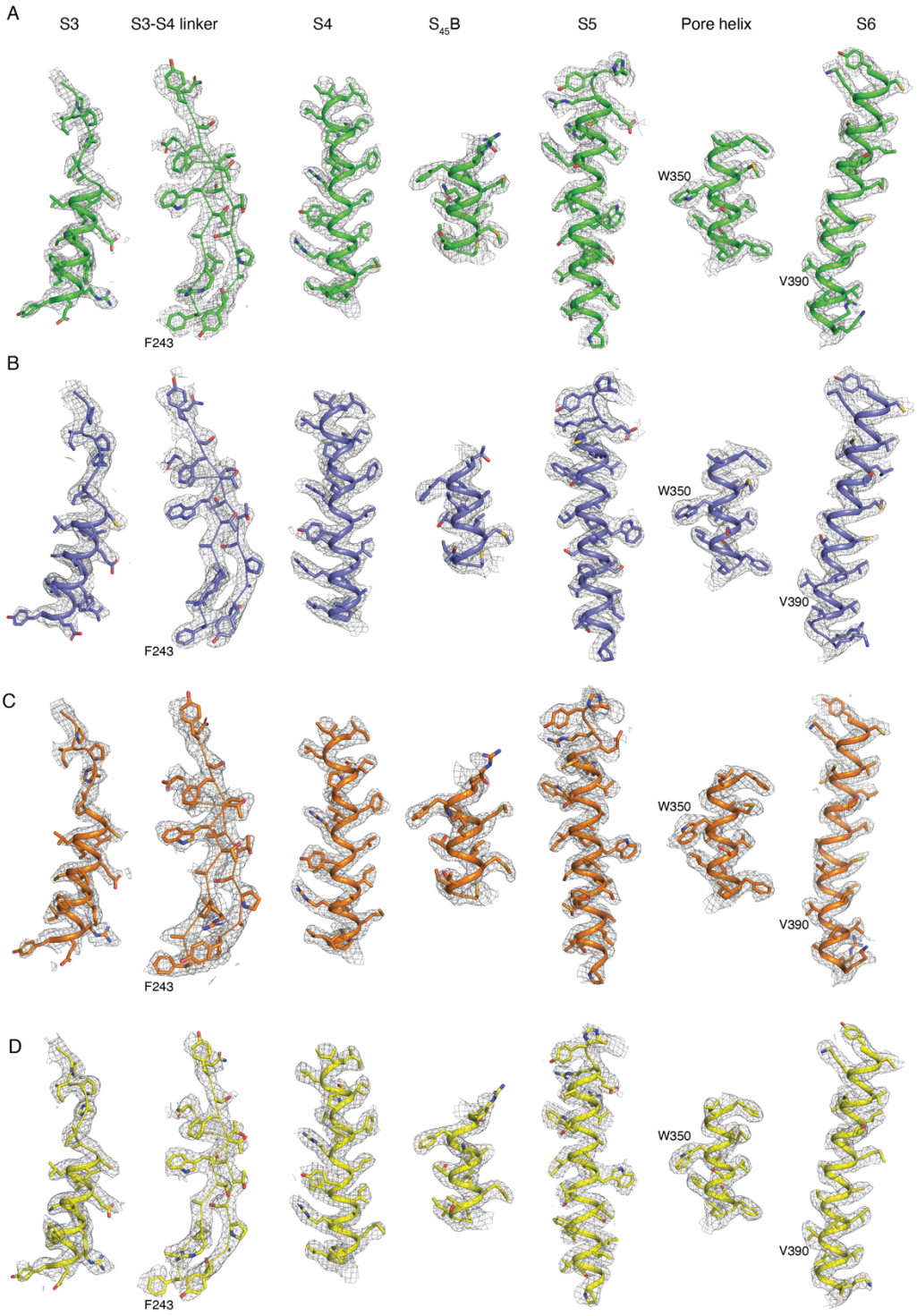

Figure S3 Representative cryo-EM densities. Cryo-EM densities of the S3, S3-S4 linker, S4, $S_{45}B$, S5, pore helix, and S6 for (A) Ca^{2+}-bound SK2-4, (B) Ca^{2+}-free SK2-4, (C) apamin-bound SK2-4, and (D) compound 1-bound SK2-4.

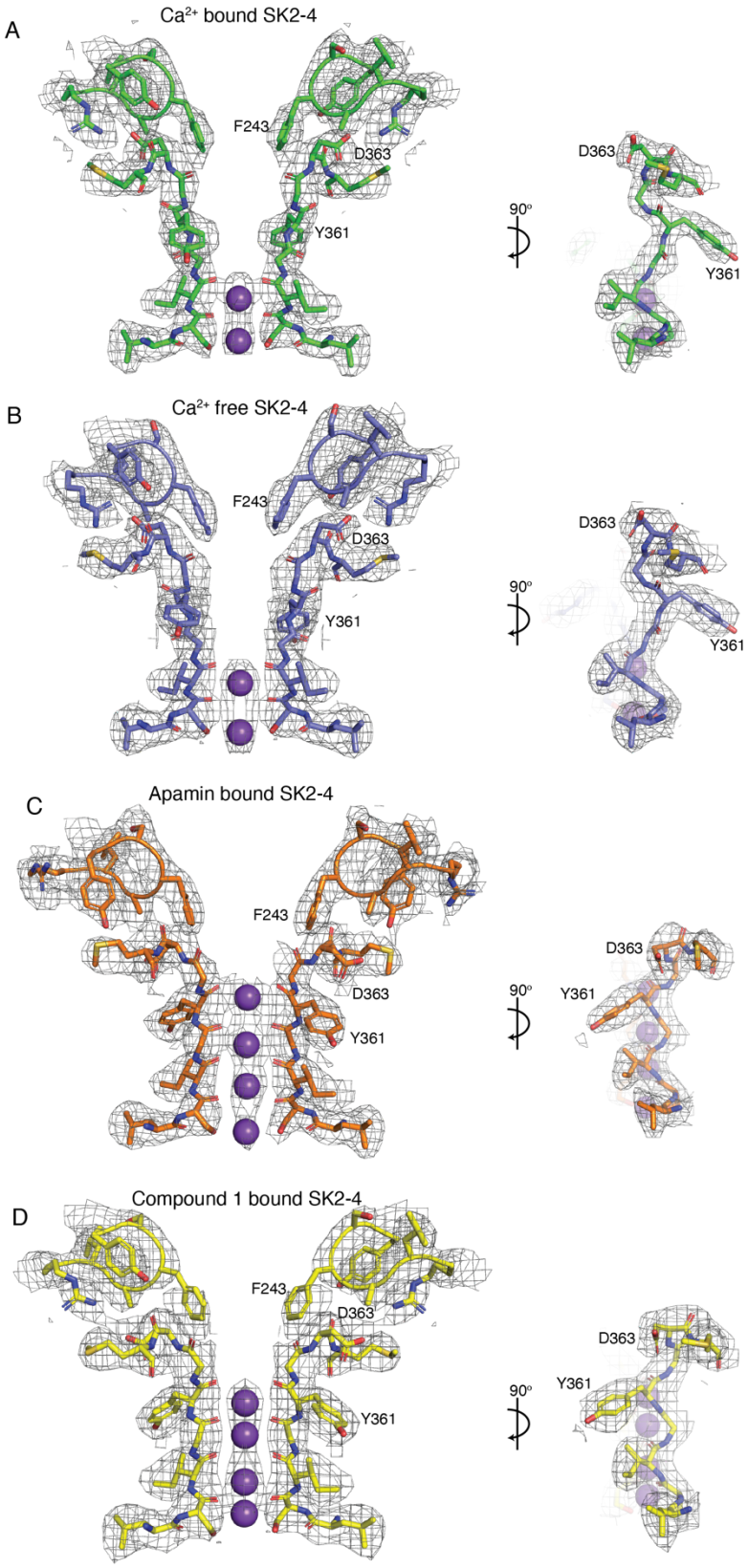
A
Ca2+ bound SK2-4
F243
D363
Y361
90°
D363
Y361
B
Ca2+ free SK2-4
F243
D363
Y361
90°
D363
Y361
C
Apamin bound SK2-4
F243
D363
Y361
90°
D363
Y361
D
Compound 1 bound SK2-4
F243
D363
Y361
90°
D363
Y361

Figure S4 Cryo-EM density for the SK2-4 selectivity filter. Cryo-EM density for the selectivity filter and interacting S3-S4 residues (not shown in 90° rotated view) for (A) Ca^{2+}-bound SK2-4, (B) Ca^{2+}-free SK2-4, (C) apamin-bound SK2-4, and (D) compound 1-bound SK2-4.

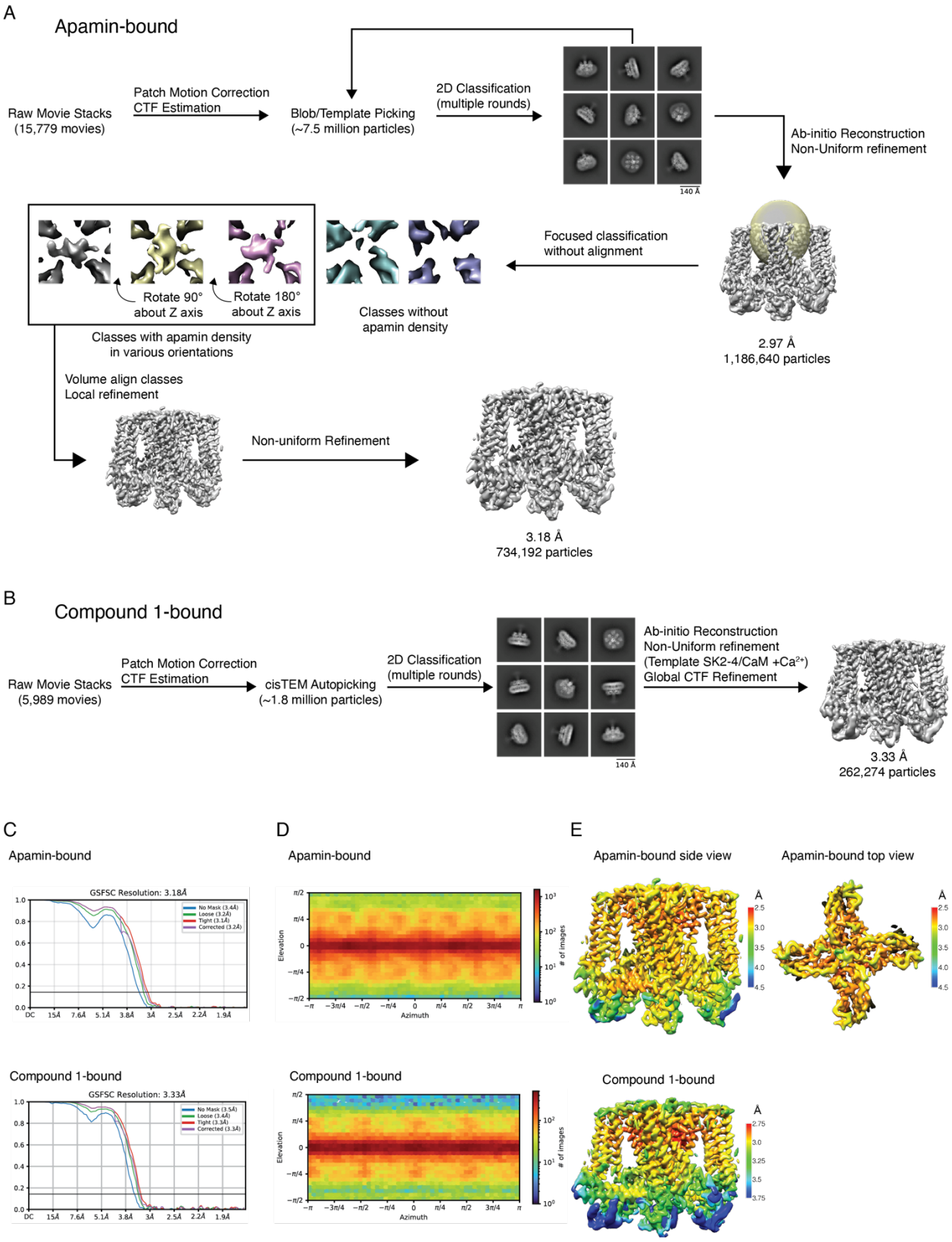

Figure S5 Structure determination of apamin-bound SK2-4 and compound 1-bound SK2-4. Cryo-EM structure determination flowchart for (A) apamin-bound SK2-4

and (B) compound 1-bound SK2-4. (C) FSC curves, (D) angular distribution, and (E) local resolution estimates for apamin-bound SK2-4 and compound 1-bound SK2-4.

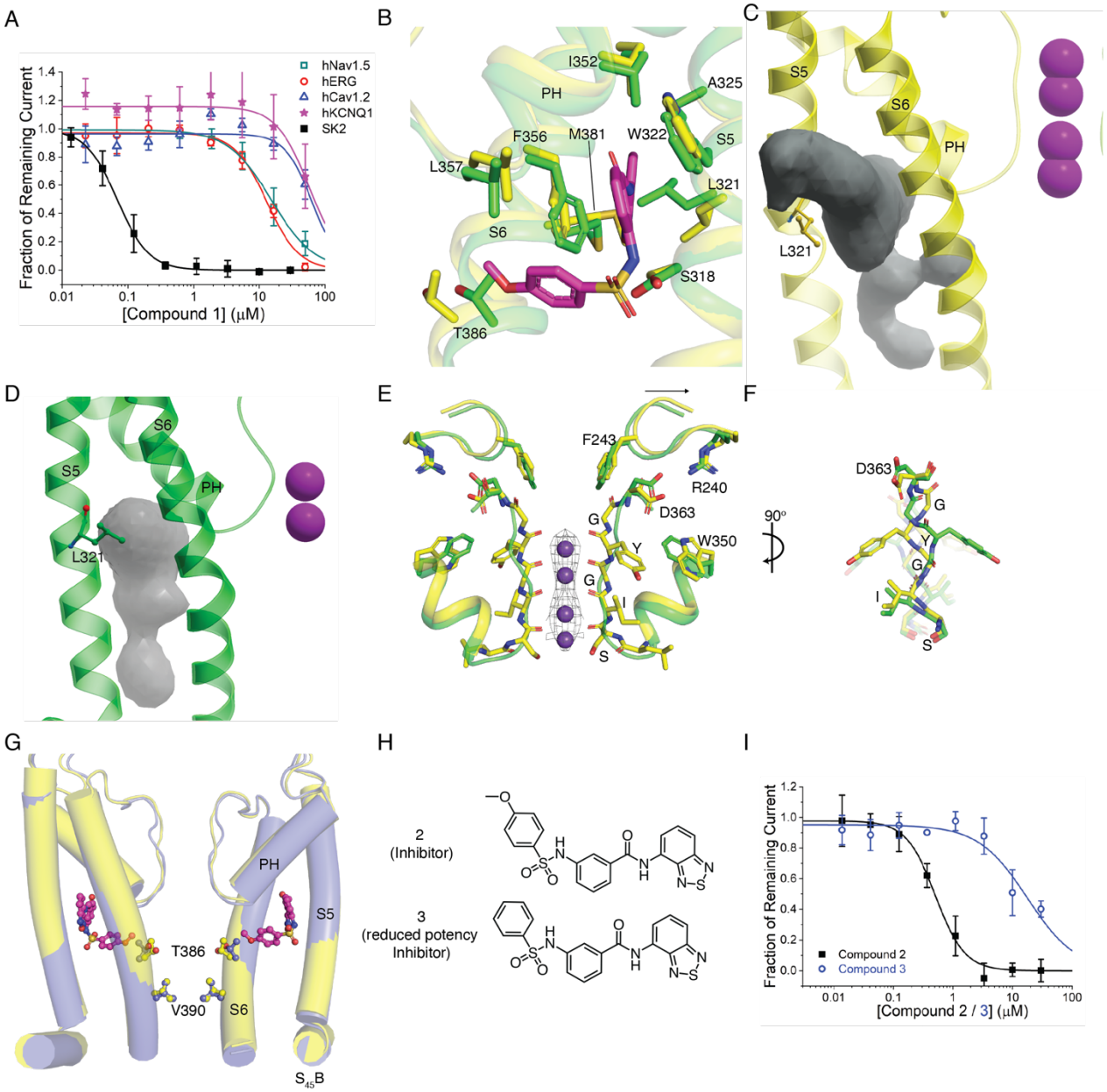

Figure S6 Characterization of compound 1 inhibition. A) Potency of compound 1 on WT SK2 (black squares, IC_{50}=69 nM), hNav1.5 (cyan squares, IC_{50}=15.3 μM), hERG (red circles, IC_{50}=13 μM), hCav1.2 (blue triangles, IC_{50} >50 μM), and hKCNQ1 channels (purple stars, IC_{50} >50 μM). Data points represent mean +/- SD (n=4-6). B) Overlay of the compound 1 (magenta sticks) binding site from the structures of compound 1-bound SK2-4 (yellow) and Ca^{2+}-bound SK2-4 (green). A rotation of Leu321 is required to accommodate the benzoxadiazole. The methoxy of compound 1 (magenta sticks) clashes with the S6 Thr386 in Ca^{2+}-bound SK2-4. Surface representation of the compound 1 binding pocket in (C) compound 1-bound SK2-4 (yellow cartoon and grey pocket) and (D) Ca^{2+}-bound SK2-4 (green cartoon and grey pocket). Rotation of Leu321 is required to expand the pocket and accommodate the benzoxadiazole of compound 1.

E) Overlay of Ca^{2+}-bound SK2-4 selectivity filter (green cartoon) and compound 1-bound SK2-4 selectivity filter (yellow, selectivity filter shown as sticks and S3-S4 linker and pore helix shown as cartoons). Upon compound 1 binding the S3-S4 linker moves away from the pore axis (black arrow) and the selectivity filter adopts a conformation with four K^+ coordination sites (purple spheres, density shown). F) 90° degree rotation of (E). G) Overlay of Ca^{2+}-free SK2-4 (lavender) and compound 1-bound SK2-4 (yellow). The S6 and $S_{45}B$ helices adopt a similar conformation in the Ca^{2+}-free and compound 1 (magenta spheres)-bound states with a closed intracellular gate (Val390, spheres). H) Structure of compound 2 and compound 3. I) Removal of the methoxy from compound 2 (black squares, IC_{50}=0.51 μM) produces compound 3 (blue circles, IC_{50}=18 μM) with a 30-fold reduction in potency. Data points represent mean +/- SD (n=6).

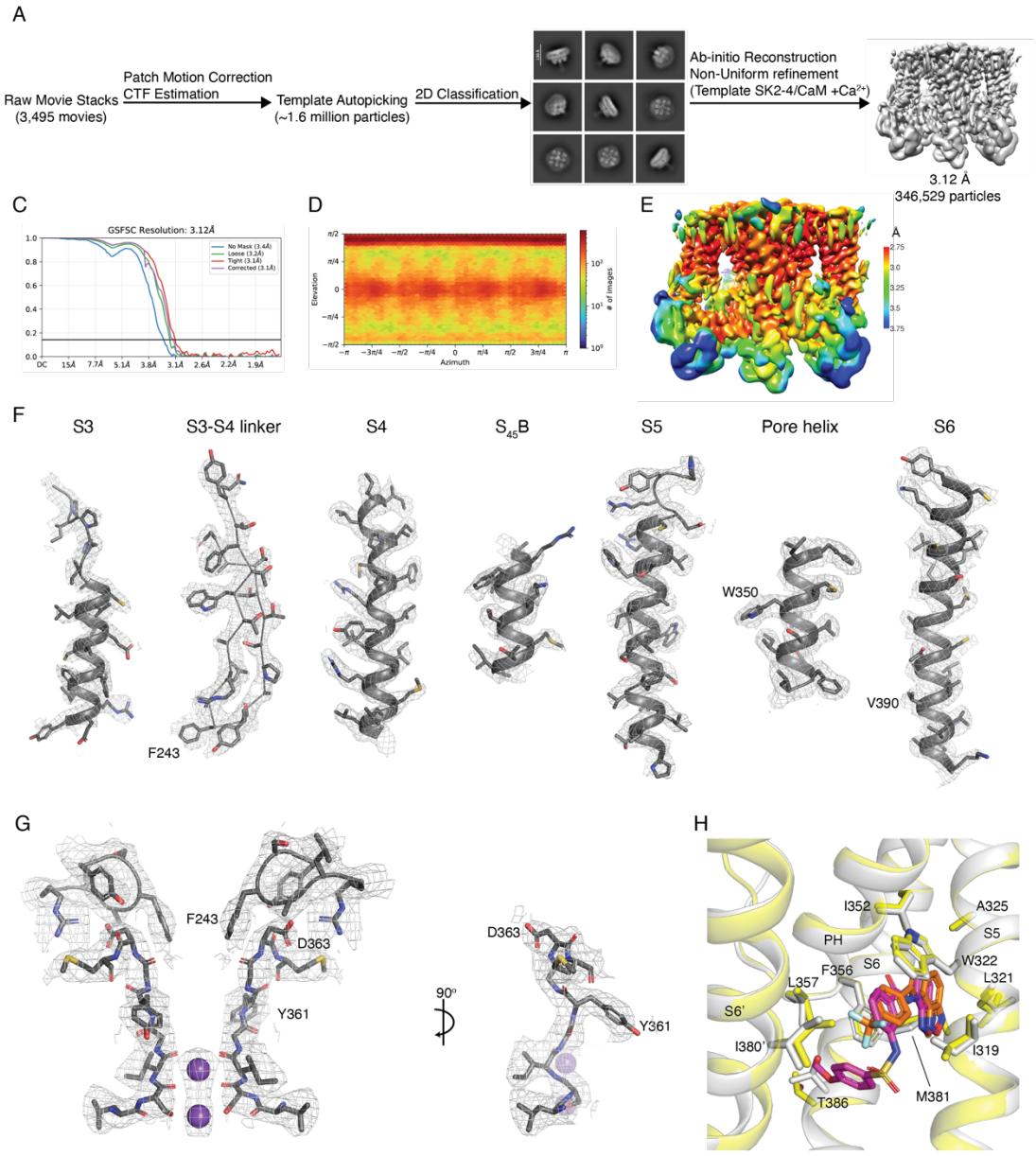

Figure S7 Structure determination of compound 4-bound SK2-4. Cryo-EM structure determination flowchart (A), FSC curves (B), angular distribution (C), and local resolution estimates (D) for compound 4-bound SK2-4. E) Cryo-EM densities of the S3, S3-S4 linker, S4, $S_{45}B$, S5, pore helix, and S6 for compound 4-bound SK2-4. D) Cryo-EM density for the selectivity filter and interacting S3-S4 residues (not shown in 90° rotated view) for compound 4-bound SK2-4. H) Overlay of compound 1 (magenta sticks) bound to SK2-4 (yellow cartoon and sticks) and compound 4 (orange sticks) bound to SK2-4 (grey cartoon and sticks).

Table S1: Data collection parameters and Refinement statistics

Structure	**SK2-4/CaM + Ca^{2+}**	**SK2-4/CaM Ca^{2+}-free**	**SK2-4/CaM + apamin**	**SK2-4/CaM + compound 1**	**SK2-4/CaM + compound 4**
PDB	9O48	9O51	9O52	9O53	9O5O
EMDB	EMD-70089	EMD-70120	EMD-70121	EMD-70122	EMD-70145
Data Collection/Processing					
Microscope	Krios	Krios	Krios	Krios	Glacios
Voltage (kV)	300	300	300	300	200
Magnification	75,000x	75,000x	75,000x	75,000x	120,000x
Nominal defocus range (μM)	-0.8 to -1.6	-0.8 to -1.6	-0.8 to -1.4	-0.8 to -1.6	-0.8 to -2.0
Pixel size (Å)	0.845	0.845	0.845	0.845	0.854
Total dose (e^-/Å^2)	50	50	50	50	35
Exposure time (s)	3	3	3.05	3	28
Micrograph number	10,123	8,928	15,779	7,300	3,495
Symmetry	C4	C4	C1	C4	C4
Initial particle number	~8.3 million	~8.2 million	~7.5 million	~1.9 million	~1.6 million
Final particle number	658,368	386,845	734,192	262,274	346,529
Map resolution (Å)	3.1	3.4	3.2	3.3	3.1
FSC threshold	0.143	0.143	0.143	0.143	0.143
Refinement					
Model Resolution (Å)	3.1	3.5	3.2	3.4	3.2
FSC threshold	0.5	0.5	0.5	0.5	0.5
Map sharpening B-factor (Å^2)	122.9	142.3	126.2	143.6	182.5
Map composition					
Non-hydrogen atoms	16,094	12,302	16,185	15,628	15,742
Protein residues	2,044	1,596	2,056	1,992	1,988
Ligands	0	0	1	4	4
B-factors (Å^2)					
Protein					
SK2-4 chains	46.72	64.36	65.19	30.84	67.53
CaM chains	93.73	145.43	107.20	86.32	134.41
Ligand	N/A	N/A	84.36	11.28	48.74
R.M.S. deviations					
Bond length (Å)	0.002	0.002	0.003	0.004	0.003
Bond angle (°)	0.354	0.400	0.465	0.457	0.5
Validation					
MolProbity score	1.11	1.05	1.06	1.19	1.34
Clashscore	3.19	2.68	2.76	4.11	6.11
Rotamers outliers (%)	0	0	0	0	0
Ramachandran plot (%)					
Favored	98.61	98.71	98.62	98.17	98.83
Allowed	1.39	1.29	1.38	1.83	1.17
Disallowed	0	0	0	0	0

Methods

Construct design

The amino acid sequences for human SK2 (KCNN2, Uniprot Q9H2S1, 579 amino acids) and human SK4 (KCNN4 Uniprot O15554, 427 amino acids) were used to design the chimeric SK2-4 channel construct. The N-terminal portion of SK2 made up of residues 1-123 was replaced with SK4 residues 1-15. The C-terminal portion of SK2 encompassing residues 413-579 was replaced with SK4 residues 306-428. On the C-terminal of this chimeric SK2-4, an HRV3C protease recognition sequence followed by GFP sequence were appended, resulting in construct SK2-4-GFP.

The amino acid sequences for SK2-4-GFP and human calmodulin (CaM) (CALM1, Uniprot P0DP23, 149 amino acids) were codon optimized using Twist Bioscience's tool to create DNA sequences for expression. These constructs were synthesized and cloned into the vector pWIL-BacMam for expression and purification. The pWIL-BacMam vector contains the Tn7 transposon and encodes a baculovirus genome with a multiple cloning site, such that when a gene of interest is placed in the pWIL-BacMam vector and transformed into *E. coli* DH10Bac competent cells (ThermoFisher Scientific) it produces bacmid containing the gene of interest. It also contains a CMV enhancer and promoter for expression of the gene of interest in mammalian cells.

SK2-4/CaM chimeric channel complex production

SK2-4 chimeric channel/CaM complex was produced using the BacMam method. Plasmids encoding the constructs (SK2-4-GFP, CaM) were each separately transformed into *E. coli* DH10Bac competent cells (ThermoFisher Scientific) following the manufacturer's protocol & plated onto blue/white selection LB agar plates (Teknova). After 2 days of incubation at 37 °C, a white colony for each construct was selected and grown overnight in 5 mL liquid medium containing 7 µg/mL gentamicin sulfate, 50 µg/mL kanamycin, and 10 µg/mL tetracycline hydrochloride (Teknova). Cells were harvested by centrifugation at 5000 x g for 5 minutes. Cell pellets were resuspended in 250 µL P1 buffer (Qiagen) and incubated briefly with 250 µL P2 buffer (Qiagen) before addition of 350 µL N3 buffer (Qiagen). Solutions were centrifuged for 10 minutes at 16,000 x g. Supernatant was added to 1 mL of ice-cold isopropanol and incubated for 20 minutes at -20 °C. Solutions were centrifuged for 15 minutes at 16,000 x g and 4 °C to pellet DNA. Supernatant was discarded and pellet was washed with 1 mL of ice-cold 70% ethanol, followed by centrifugation at 16,000 x g for 10 minutes. Supernatant was discarded and pellet was left to air-dry for 10 minutes before resuspension with 50 µL of molecular-biology grade water.

Baculovirus for each construct was produced by transfection of bacmid into SF9 cells as follows: 3 µL X-tremeGENE HP DNA transfection reagent (Roche), 5 µL of bacmid, and 100 µL transfection medium (Expression Systems) were incubated for 15 minutes at

room temperature. After incubation, 2.5 mL of Sf9 insect cells (Expression Systems) at a density of 1 million cells/mL were added. Cells were incubated for 1 week with shaking at 27 °C before baculovirus-containing medium was harvested. Baculovirus was amplified in Sf9 cells for two additional rounds after transfection. Expi293F cells (ThermoFisher Scientific) were grown in suspension at 37 °C in 8% CO_2 atmosphere with 110 rpm shaking to a density of approximately 3 x 10^6 cells/mL before transduction with virus. Virus was added to the culture with 2% v/v CaM baculovirus and 8% v/v of SK2-4-GFP baculovirus. Approximately 16 hours after transduction, sodium butyrate was added to cultures to a final concentration of 10 mM. Cultures were incubated an additional ~48 hours at 37 °C in 8% CO_2 atmosphere with 110 rpm shaking before harvest by centrifugation at 6,000 x g for 45 minutes. Cell pellets were flash-frozen in liquid nitrogen and stored at -80 °C until use.

Cell pellet from a 4 L culture was resuspended in 200 mL of room-temperature resuspension buffer (10 mM Tris pH 8, 20 mM KCl, 2 mM $CaCl_2$, 0.5 mM $MgCl_2$, 0.05 mg/mL DNase I, Pierce protease inhibitor tablet EDTA-free) for 30 minutes with vigorous stirring. Lysate was centrifuged for 45 minutes at 35,500 x g to collect membranes. The membrane pellet was resuspended in 200 mL of extraction buffer (10 mM Tris pH 8, 20 mM KCl, 2 mM $CaCl_2$, 2% w/v DDM, 0.4% w/v CHS, Pierce protease inhibitor tablet EDTA-free) using a dounce. Membranes were solubilized with vigorous stirring at 4 °C for 2 hours. Solution was clarified by ultracentrifugation at 195,000 x g for 1 hour at 4 °C.

Supernatant was incubated with 4 mL GFP nanobody resin (Bulldog Bio) pre-equilibrated with wash buffer (20 mM Tris pH 8, 150 mM KCl, 2 mM $CaCl_2$, 0.05% w/v n-dodecyl-β-D-maltopyranoside (DDM), 0.01% w/v cholesteryl hemisuccinate tris salt (CHS)) for 1.5 hours at 4 °C with gentle agitation. Resin was collected over a gravity column and washed with 5 column volumes (CV) of wash buffer supplemented with 5 mM ATP and 10 mM $MgCl_2$, followed by washing with 10 CV of unsupplemented wash buffer. Resin was resuspended in 20 mL of wash buffer with 0.25 mg of HRV3C protease and incubated overnight at 4 °C with gentle agitation to cleave untagged SK2-4/CaM complex from the resin. Supernatant containing protein was collected and concentrated to 0.5 mL using 100 kDa MWCO Amicon Ultra centrifugal filter (EMD Millipore).

Concentrated protein was applied to a Superose 6 Increase 10/300 GL column (Cytiva) pre-equilibrated with SEC buffer. For samples purified in presence of Ca^{2+}, the SEC buffer was 20 mM Tris pH 8, 150 mM KCl, 2 mM $CaCl_2$, 0.005% w/v glyco-diosgenin (GDN), 0.0005% w/v CHS. For Samples purified in absence of Ca^{2+}, the SEC buffer was 20 mM Tris pH 8, 150 mM KCl, 5 mM EGTA, 0.005% w/v GDN, 0.0005% w/v CHS. Size exclusion was performed at 4 °C with a flow rate of 0.5 mL/minute. SDS-PAGE was performed using NuPAGE Bis-tris 4-12% gel (Invitrogen) and NuPAGE MES SDS running buffer (Invitrogen) to identify fractions with pure SK-4/CaM complex. Fractions were collected and concentrated using 100 kDa MWCO Amicon Ultra centrifugal filter to desired concentration and frozen directly onto cryo-EM grids.

EM sample preparation and data collection

SK2-4/CaM complex samples were prepared at the following concentrations: Ca^{2+}-bound SK2-4/CaM at 7.5 mg/mL; Ca^{2+}-free SK2-4/CaM at 8.25 mg/mL. For samples with apamin present, Ca^{2+}-bound SK2-4/CaM was supplemented with apamin (Sigma-Aldrich) to a final concentration of 200 μM. For the sample with compound 1, Ca^{2+}-bound SK2-4/CaM was supplemented with compound 1 in 100% DMSO to a final concentration of 200 μM compound 1 and 2% DMSO. For the sample with compound 4, Ca^{2+}-bound SK2-4/CaM was supplemented with compound 4 in 100% DMSO to a final concentration of 500 μM compound 4 and 2% DMSO.

UltrAuFoil® R 0.4/1.2 200 mesh grids were used for the Ca^{2+}-bound and Ca^{2+}-free SK2-4/CaM samples and UltrAuFoil® R 1.2/1.3 300 mesh grids were used for all other samples. The grids (Electron Microscopy Sciences) were glow-discharged for 30 seconds at 0.5 mBar with 15 mA using easiGlow system (PELCO). 5 μL of sample were applied to grids at 4°C with 100% humidity. After 30 seconds, grids were blotted for 5 seconds with blot force 25 and plunged into liquid ethane using the Vitrobot Mark IV system (Thermo Fisher).

For Ca^{2+}-bound SK2-4/CaM, Ca^{2+}-free SK2-4/CaM, SK2-4/CaM + Apamin, and Ca^{2+}-bound SK2-4/CaM + compound 1, data were collected on a Titan Krios microscope (Thermo Fisher Scientific, Waltham, MA, USA) equipped with a Cs-corrector hardware operated at an accelerating voltage of 300 kV with a 50 μm C2 aperture at an indicated magnification of 75,000× in nanoprobe mode. A Falcon4i Direct Electron Detector camera operated in Electron-Event representation (EER) mode electron was used to acquire dose-fractionated images with Thermo Fisher Scientific EPU software. For Ca^{2+}-bound SK2-4/CaM + compound 4, data were collected on a Glacios microscope (Thermo Fisher Scientific, Waltham, MA, USA) operated at an accelerating voltage of 200 kV with a 50 μm C2 aperture at an indicated magnification of 120,000× in nanoprobe mode. A Falcon3 Direct Electron Detector camera was used to acquire dose-fractionated images with Thermo Fisher Scientific EPU software. Data collection parameters for each data set are listed in table S1.

EM data processing

[Ca^{2+}-bound SK2-4/CaM] Movie stacks were gain-corrected and motion-corrected in patches using MotionCor2[47]. Motion-corrected images were imported into cryoSPARC4[48]. Contrast transfer function parameters were determined using Patch CTF. Blob picking was performed with a subset of the micrographs with an expected diameter of 160 to 180 Å. Selected particles were extracted with a box size of 360 pixels and subjected to reference-free 2D classification to generate templates, which were used for subsequent template-based autopicking with the full set of micrographs. 8,310,008 particles were selected and extracted with a box size of 360 pixels. After iterative rounds of reference-free 2D classification 910,204 particles were used to

generate two *ab initio* models. The 658,368 particles from the better model were subjected to non-uniform 3D refinement[49] with imposed C4 symmetry using the *ab initio* model as a template resulting in a 3.1 Å consensus refinement. After local CTF refinement, a soft mask excluding the detergent micelle was generated for local refinement with imposed C4 symmetry, resulting in the final consensus refinement with a resolution of 3.1 Å.

[Ca^{2+}-free SK2-4/CaM] Movie stacks were gain-corrected and motion-corrected in patches using MotionCor2[47]. Motion-corrected images were imported into cryoSPARC4[48]. Contrast transfer function parameters were determined using Patch CTF. Blob picking was performed with a subset of the micrographs with an expected diameter of 160 to 180 Å. Selected particles were extracted with a box size of 360 pixels and subjected to reference-free 2D classification to generate templates, which were used for subsequent template-based autopicking with the full set of micrographs. 8,160,096 particles were selected and extracted with a box size of 360 pixels. After iterative rounds of reference-free 2D classification 386,845 particles were subjected to non-uniform 3D refinement[49] with imposed C4 symmetry using the Ca^{2+}-bound SK2-4/CaM consensus refinement as a template, resulting in a 3.4 Å consensus refinement. A soft mask excluding the detergent micelle and the intracellular stalk was generated for local refinement with imposed C4 symmetry, resulting in the final consensus refinement with a resolution of 3.4 Å.

[SK2-4/CaM + Apamin] Movie stacks were gain-corrected and motion-corrected in patches using MotionCor2[47]. Motion-corrected images were imported into cryoSPARC4[48]. Contrast transfer function parameters were determined using Patch CTF. Template autopicking was performed using the 2D class averages from the SK2-4/CaM + Ca^{2+} data set. 7,528,863 picked particles were extracted using a box size of 360 pixels. Iterative rounds of reference-free 2D classification led to 1,440,270 particles which were used to generate two *ab initio* models. The better model comprising of 1,186,640 particles was subjected to non-uniform refinement[49] using the *ab initio* model as a template, first with C4 symmetry imposed, which led to a consensus refinement at 3 Å. Density at the top of the SK2-4 pore was identified as the likely apamin binding site. A soft ovoid mask covering the top of the pore and the SK2-4 selectivity filter was used for focused 3D classification without alignment of the particles with C1 symmetry and five classes. Three classes comprising of 734,192 total particles had clear asymmetrical density for apamin at the extracellular opening of the pore. The classes appeared to be structurally identical but rotated by 90° from one another. Volume alignment tools were used to rotate the volumes and associated particle stacks 90° or 180° around the symmetry axis so the three classes were in the same orientation. These particle stacks were put into a local refinement with C1 symmetry using one of the classes as a template and with a soft mask that excluded the detergent micelle and intracellular stalk of SK2-4, resulting in a consensus refinement at 3.1 Å with clear density for apamin at

the extracellular pore opening. This was followed by a non-uniform refinement with C1 symmetry with the local refinement map used as a template, resulting in a final consensus refinement at 3.2 Å.

[Ca^{2+}-bound SK2-4/CaM + compound 1] Movie stacks were gain-corrected and motion-corrected in patches using MotionCor2[47]. Motion-corrected images were imported into cisTEM[50] for contrast transfer function estimation followed by particle picking. 1,884,323 selected particles were extracted with a box size of 360 pixels and subsequently imported into cryoSPARC4[48]. Reference-free 2D classification was performed to select 326,099 good particles. These were used to generate two *ab initio* models. The better model comprising of 262,274 particles was subjected to non-uniform refinement[49] using the Ca^{2+}-bound SK2-4/CaM model as a template, resulting in a consensus refinement at 3.3 Å. This refinement was put through global CTF refinement, followed by another round of non-uniform refinement resulting in the final map at 3.3 Å.

[Ca^{2+}-bound SK2-4/CaM + compound 4] Movie stacks were gain-corrected and motion-corrected in patches using MotionCor2[47]. Motion-corrected images were imported into cryoSPARC4[48]. Contrast transfer function parameters were determined using Patch CTF. Template-based autopicking, extraction with a box size of 360 pixels, and reference-free 2D classification were performed to select 436,179 good particles. These were used to generate two *ab initio* models. The better model comprising of 360,727 particles was subjected to non-uniform refinement[49] using the Ca^{2+}-bound SK2-4/CaM model as a template, resulting in a consensus refinement at 3.1 Å.

Model building

For the Ca^{2+}-bound SK2-4/CaM structure, the SK2-4 region was built *de novo* in Coot[51] using the 3.1 Å -EM density map. For CaM, a chain of CaM from the cryo-EM structure 6CNN was docked into the cryo-EM map in Chimera[52], followed by adjustment in Coot. 4-fold symmetry was enforced on the model in Coot. The model was refined against the cryo-EM density map using iterative rounds of manual adjustment in Coot followed by refinement in Phenix[53].

For the model building of the Ca^{2+}-free SK2-4/CaM, apamin-bound, compound 1-bound, and compound-4 bound structures the Ca^{2+}-bound SK2-4/CaM structure was used as a starting point and manually docked into the corresponding cryo-EM density maps, followed by manual adjustment in Coot[51]. For the apamin-bound structure, apamin from the NMR structure 7OXF was docked into the cryo-EM density map using Chimera[52], followed by truncation of unresolved regions and manual adjustment in Coot. For the Ca^{2+}-free and compound 1-bound structures, 4-fold symmetry was enforced in Coot. No symmetry was enforced for the apamin-bound model. The models were refined against their respective cryo-EM density maps using iterative rounds of manual adjustment in Coot followed by refinement in Phenix[53].

For all models, if the backbone was not visible in the density map, the residue was not modeled. Residues with poorly-defined sidechain density were truncated at Cβ. The quality of the models was determined using MolProbity[54]. Figures were prepared using PyMOL (Schrödinger, LLC. 2010. The PyMOL Molecular Graphics System, Version 3.1.3) and Chimera[52].

Electrophysiology assays

SK channel assays: All electrophysiology assays for SK used CHO-K1 cells either stably expressing SK channels (WT SK2 and SK4) or transiently transduced with channel baculovirus constructs (WT & mutant SK2, SK4 and SK2-4 chimera) using the BacMam system. Stably channel-expressing cells were cultured using T150 flasks in 37 °C incubator with 5% CO_2 until 70-80% confluency. Culture media were composed of Dulbecco's modified Eagle's medium/F-12 nutrient mixture (DMEM/F-12, #31320, Gibco) and 10% fetal bovine serum (#89510-196, Avantor), 1% penicillin/streptomycin (#15140, Gibco) and 1% non-essential amino acids (#11140, Gibco). For BacMam transduction, 8 million parental CHO-K1 cells were seeded into a T150 flask with 15 mL media. After >6 hours in 37 °C incubator with 5% CO_2 and until cells were attached, media were aspirated and replaced with 10 mL fresh media containing 400 µL baculovirus for individual channel constructs. After this, cells were cultured in 30 °C incubator with 5% CO_2. After overnight media were aspirated and replaced with 10 mL media containing 4 µM Tricostatin A (#T-1952, Sigma) for 4 hours before dilution to 1 µM by adding 30 mL media. Cells were ready to use >40 hours in 30 °C incubator after transduction. On the day of experiments for all cells, media were aspirated before a wash with PBS (#14190, Gibco). Cells were then dissociated using 5 mL TryplE (#12605010, ThermoFisher) for 3 min at 37 °C, spun down and resuspended in serum free medium (#12052114, Gibco) with added 25 mM HEPES (#15630, Gibco). Right before experiments, cells were spun down again and resuspended in extracellular buffer containing 5 mM $BaCl_2$ at 2-3 million cells/mL before loaded to the "cell transfer plate" of the Qube instrument (Sophion).

All SK electrophysiological recordings were made with the automated Qube system and 384X 10-hole QChips at 22 °C. Sum of SK currents from up to 10 cells are measured in each recording well from the 384-well plate. Briefly, cells from Qube "cell transfer plate" were pipetted into each well to form seals then broken into whole-cell configuration. Extracellular buffer contains (in mM): 130 NaCl, 6 KCl, 2 $CaCl_2$, 40 sucrose, 10 HEPES, 1 $MgCl_2$, pH=7.4 with NaOH. To enhance sealing, 5 or 15 mM $BaCl_2$ were added to extracellular buffer (sucrose reduced accordingly to maintain osmolarity) which were washed away with Ba^{2+} free extracellular buffer after seal was formed. Intracellular buffer contains (in mM): 110 K_2SO_4, 8 NaCl, 4.68 $CaCl_2$, 10 HEPES, 5 EGTA, 5 HEDTA, and 4 Mg-ATP added right before experiments, pH=7.0 with KOH. SK current was recorded using a 250 ms long voltage ramp from -120 mV to +80 mV, whereas current level at ~0 mV was taken as the current amplitude to minimize contribution by leak. No series resistance compensation or leak subtraction was included in voltage protocol. For

pharmacological effects, cells were washed with Ba^{2+} free extracellular buffer containing different concentrations of compounds before SK currents were recorded (a single concentration per well). Leak and non-SK currents were estimated at the end of experiment with saturating concentration of specific SK inhibitors (10 μM UCL1684 ,30 μM AP14145, or 10 μM TRAM-34, as needed) and subtracted from average current amplitudes. Average current amplitude after compound from each well was normalized to its before-compound amplitude then normalized to time-matched wells treated with 0.3% DMSO. Normalized values at each concentration (n=4-6 wells) were used to construct dose response curves, which were fitted with Hill Equation to yield IC_{50} values. For Ca^{2+} dependent activation of SK channels, different amounts of $CaCl_2$ were added to intracellular buffer to achieve desired levels of free Ca^{2+} concentration (determined by online MaxChelator program at https://somapp.ucdmc.ucdavis.edu/pharmacology/bers/maxchelator/webmaxc/webmaxcE.htm). On a 384-well plate, each 24 wells (3 columns) were exposed to intracellular buffer containing one of eight different calculated free Ca^{2+} concentrations ranging from 0.1 to 20 μM. Average SK current amplitudes from 24 wells for each [Ca^{2+}] were normalized to level at 20 μM and plotted against free Ca^{2+} concentration to construct the Ca^{2+} dependent activation curve, which was fitted with the Hill Equation to yield EC_{50} values. Note that on the automated high throughput electrophysiology system, it is only feasible to record current in whole-cell configuration (in contrast to inside-out) in which true intracellular free [Ca^{2+}] may differ from the calculated values for the bulk intracellular buffers due to incomplete dialysis.

Counter-screening assays on other ion channels. Compound effect on hERG channel was tested on the Qube system at 35 °C using CHO-K1 cells stably expressing hERG channel. Assay conditions were similar as the SK assay except for buffers and voltage protocol. Extracellular buffer contains (in mM): 145 NaCl, 4 KCl, 2 $CaCl_2$, 10 glucose, 10 HEPES, 1 $MgCl_2$, pH=7.4 with NaOH. Intracellular buffer contains (in mM): 20 KCl, 120 KF, 10 EGTA, 10 HEPES, pH=7.2 with KOH. hERG channel inhibition was measured by peak tail current level at -50 mV after a 3.5-sec long depolarization to 10 mV. Compound effect on hCav1.2 channel was tested on the Qube system at 35 °C using CHO-K1 cells expressing hCav1.2 channel (inducible with the T-Rex system). Assay conditions were similar as the SK assay except for buffers and voltage protocol. Extracellular buffer contains (in mM): 145 NaCl, 10 $CaCl_2$, 10 HEPES, 4 KCl, pH=7.4 with NaOH. Intracellular buffer contains (in mM): 112 CsCl, 28 CsF, 2 NaCl, 10 HEPES, 8.2 EGTA, pH=7.3 with CsOH. Cav1.2 channel inhibition was measured by peak current level at 10 mV depolarization from a -70 mV holding potential. Compound effect on hKCNQ1 channel was tested on the Qube system at 22 ºC using CHO-K1 cells stably expressing hKCNQ1 channel. Assay conditions were similar as the SK assay except for voltage protocol. Extracellular buffer contains (in mM): 130 NaCl, 6 KCl, 2 $CaCl_2$, 40 sucrose, 10 HEPES, 1 $MgCl_2$, pH=7.4 with NaOH. Intracellular buffer contains (in mM) 110 K_2SO_4, 8 NaCl, 4.68 $CaCl_2$, 10 HEPES, 5 EGTA, 5 HEDTA and 4 Mg-ATP added right before

experiments, pH=7.0 with KOH. hKCNQ1 channel inhibition was measured by peak current level at 4-sec long depolarization to 50 mV from a -80 mV holding potential. Compound effect on hNav1.5 channel was tested on the QPatch (Sophion) system at room temperature using CHO-K1 cells stably expressing hNav1.5 channel. QPatch is a different automated electrophysiology system than the Qube and uses 48-well plates. Extracellular buffer contains (in mM): 137 NaCl, 4 KCl, 1 $MgCl_2$, 1.8 $CaCl_2$, 10 HEPES, 10 Glucose, pH=7.3 with NaOH. Intracellular buffer contains (in mM): 120 CsF, 20 CsCl, 10 HEPES, 5 EGTA, 10 NaCl, pH=7.2 with CsOH. hNav1.5 channel inhibition was measured by steady-state peak current level at -10 mV depolarization of 400 ms at 1 Hz from a holding potential of -80 mV. In contrast to Qube assays, compound effect was tested by perfusing individual cells with compounds of increasing concentrations to construct cumulative dose response curves. All dose response data points were normalized to time matched wells / cells treated with DMSO. Dose response curves were plotted as mean +/- SD and fitted with the Hill Equation.

Differential Scanning Fluorimetry assay

Differential scanning fluorimetry (DSF) assay was performed in DSF assay buffer (20 mM Tris pH 8, 150 mM KCl, 2 mM $CaCl_2$, 0.005% w/v GDN, 0.0005% w/v CHS). SK2-4/CaM complex in DSF assay buffer was prepared at a concentration of 0.042 mg/mL. compound 1 was dissolved in 100% DMSO at 10 mM before being diluted into the DSF assay buffer to 200 μM, with a final DMSO concentration of 2%. A negative control solution was prepared in the same way using only DMSO in the absence of compound. 7-Diethylamino-3-(4'-Maleimidylphenyl)-4-Methylcoumarin (CPM) was dissolved in 100% DMSO to a concentration of 4 mg/mL before being diluted into the DSF assay buffer to a concentration of 0.2 mg/mL.

Assay wells were prepared in triplicate by adding 30 μL of the SK2-4/CaM solution, 30 μL of the compound 1 solution or negative control solution, and 5 μL of the CPM solution together in Mx300P 96-well non-skirted plates (Agilent Technologies) such that each well contained 1.25 μg of SK2-4/CaM complex and 100 μM of compound 1, if present. Combined solution was briefly mixed followed by centrifugation. Plate was analyzed using Stratagene Mx3005P (Agilent Technologies) with the following method: temperature was held at 25 °C for 30 minutes, followed by an increase of 0.5 °C every 30 seconds until the temperature reached 95 °C. Fluorescence readings were taken at each temperature.

Raw data were analyzed by fitting melt curves using an extended Boltzmann function to determine melting temperature T_m for each replicate. Reported ΔT_m was determined by taking the mean of the three replicates for the compound 1 samples and subtracting the mean of the three replicates for the apo samples.

Chemical synthesis of compound 1 (N-(benzo[c][1,2,5]oxadiazol-4-yl)-3-((4-methoxyphenyl)sulfonamido)benzamide) and compound 4 (N-(benzo[c][1,2,5]oxadiazol-4-yl)-4-(trifluoromethyl)benzamide)

General methods

Unless otherwise noted, reagents and solvents were used as received from commercial suppliers. Compounds **2** and **3** were purchased from commercial suppliers. Proton nuclear magnetic resonance (NMR) spectra were obtained on either a Bruker Avance spectrometer or a Varian Oxford 400 MHz spectrometer unless otherwise noted. NMR spectra are given in ppm (δ) and coupling constants, *J*, are reported in Hertz. Tetramethylsilane (TMS) was used as an internal standard. Chemical shifts are reported in ppm relative to dimethyl sulfoxide (δ 2.50), methanol (δ 3.31), chloroform (δ 7.26) or other solvent as indicated in NMR spectral data. Peaks are reported as (s = singlet, d = doublet, t = triplet, q = quartet, m = multiplet or unresolved, br = broad signal, coupling constant(s) in Hz, integration). ^{13}C NMR spectra were recorded with ^{1}H-decoupling on Bruker AV 101 MHz spectrometers and are reported in ppm with the solvent resonance employed as the internal standard (DMSO-*d6* at 39.52 ppm). Mass spectra (ESI-MS) were collected using a Waters System (Acquity UPLC and a Micromass ZQ mass spectrometer) or Agilent-1260 Infinity (6120 Quadrupole); all masses reported are the *m*/*z* of the protonated parent ions unless recorded otherwise. The chemical names were generated using ChemDraw Professional v23 from Perkin Elmer Informatics. Temperatures are given in degrees Celsius. If not mentioned otherwise, all evaporations are performed under reduced pressure, typically between about 15 mm Hg and 100 mm Hg (= 20-133 mbar).

Synthetic scheme for N-(benzo[c][1,2,5]oxadiazol-4-yl)-3-((4-methoxyphenyl) sulfonamido) benzamide (1)

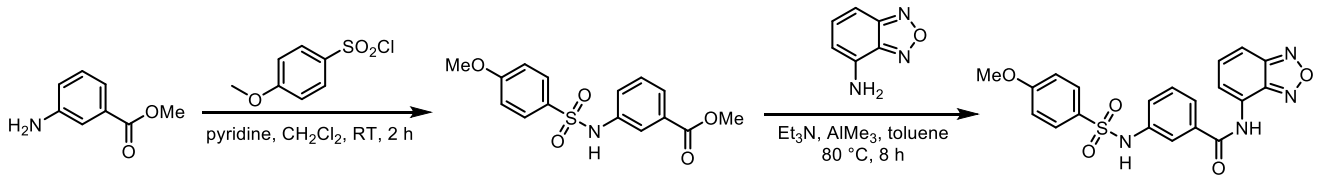

Synthesis of methyl 3-((4-methoxyphenyl)sulfonamido)benzoate

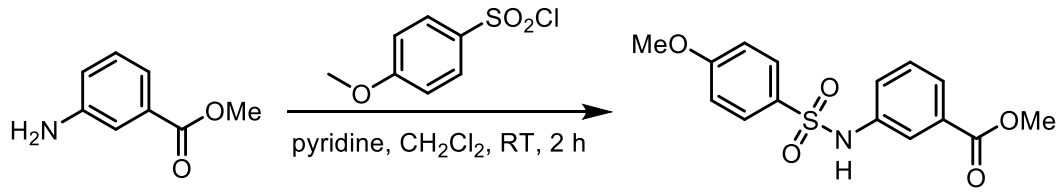

To a stirred solution of methyl 3-aminobenzoate (2.0 g, 1.0 equiv, 13.2 mmol) in DCM (10.0 mL) was added pyridine (3.14 g, 3.21 mL, 3 equiv, 39.7 mmol), followed by dropwise addition of 4-methoxybenzenesulfonyl chloride (3.28 g, 1.2 equiv, 15.6 mmol) at 25 °C. Upon complete addition, the reaction mixture was stirred at RT for 2 h. The progress of the reaction was monitored by TLC and LCMS. Upon completion of the reaction, the reaction mixture was diluted with water and extracted with DCM twice. The combined organic layers were washed with ice water twice, washed with brine, dried over Na_2SO_4, filtered, and concentrated under reduced pressure to obtain a residue. The crude residue was triturated with n-pentane and diethyl ether to get methyl 3-((4-methoxyphenyl)sulfonamido)benzoate (3.0 g, 9.1 mmol, 69% yield) as a brown solid.

LCMS

System: Shimadzu–LCMS 2020 (single quad)

Column: ACQUITY UPLC BEH C18 1.7 µm, 2.1*50 mm

Column temperature: 40 °C

Gradient (Time (min.) / %B): 0.01/2, 0.08/2, 1.50/50, 2.20/98, 3.60/98, 4.20/2, 5.00/2

Eluent A: 0.1% HCOOH in water

Eluent B: 0.1% HCOOH in CH_3CN

Flow: 0.8 mL/min

ESI-MS, negative mode, *m/z* 320.1 $[M–H]^–$, Rt: 3.25 min, 99%.

HPLC

Column: PRUDENT C18 150X4.6 mm, 5 µm

Flow: 1.0 mL/min

Mobile phase: (A) 0.01% TFA in water, (B) ACN

Gradient: T/%B 0/30, 1/70, 6/100, 8/100, 10/30, 12/30

Rt: 4.88 min, 98%

^{1}H NMR (400 MHz, DMSO-d6) δ = 10.42 (s, 1H), 7.71 - 7.68 (m, 3H), 7.63 - 7.57 (m, 1H), 7.41 – 7.35 (m, 2H), 7.10 – 7.0 (m, 2H), 3.79 (s, 3H), 3.76 (s, 3H).

Synthesis of N-(benzo[c][1,2,5]oxadiazol-4-yl)-3-((4-methoxyphenyl)sulfonamido) benzamide (1)

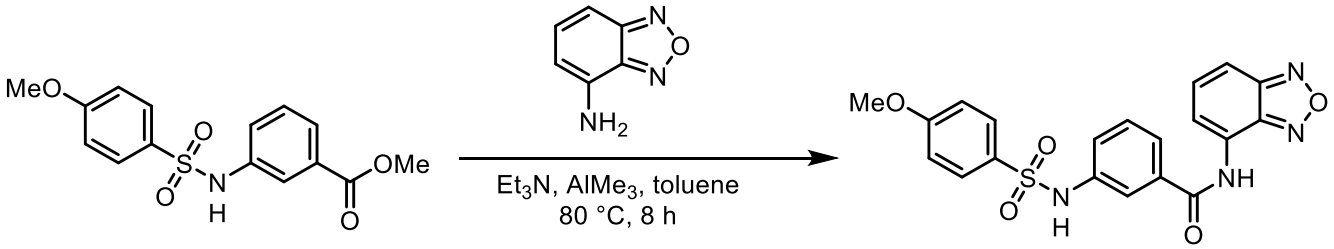

To a stirred mixture of methyl 3-((4-methoxyphenyl)sulfonamido)benzoate (500 mg, 1.0 equiv, 1.56 mmol) in toluene (5 mL) was added triethylamine (315 mg, 434 µL, 2 equiv, 3.11 mmol) and benzo[c][1,2,5]oxadiazol-4-amine (252 mg, 1.2 equiv, 1.87 mmol) followed by dropwise addition of trimethylaluminum (2M in hexane) (336 mg, 447 µL, 3 equiv, 4.67 mmol) at RT. After complete addition the reaction mixture was heated at 80 °C for 8 h. The progress of the reaction was monitored by LCMS and TLC. The reaction mixture was cooled to RT and quenched with ice water and extracted with ethyl acetate twice. The combined organic layers were washed with brine, dried over Na_2SO_4, filtered and concentrated to obtain a crude residue. The crude product was purified by normal phase silica gel chromatography, eluting with 10-25% ethyl acetate in hexane. The pure fractions were pooled and concentrated to obtain the product as a dark yellow gummy mass which was triturated with n-pentane and diethyl ether to afford N-(benzo[c][1,2,5]oxadiazol-4-yl)-3-((4-methoxyphenyl)sulfonamido)benzamide (**1**) (260 mg, 0.60 mmol, 39% yield) as a yellow solid.

LCMS

System: Shimadzu–LCMS 2020 (single quad)

Column: ACQUITY UPLC BEH C18 1.7 µm, 2.1*50 mm

Column temperature: 40 °C

Gradient (Time (min.) / %B): 0.01/2, 0.08/2, 1.50/50, 2.20/98, 3.60/98, 4.20/2, 5.00/2

Eluent A: 0.1% HCOOH in water

Eluent B: 0.1% HCOOH in CH_3CN

Flow: 0.8 mL/min

ESI-MS *m/z* 424.9, $[M+H]^+$, Rt: 2.92 min, 99%

HPLC

Column : X BRIDGE C18 150X4.6 mm, 3.5 µm

Flow: 1.0 mL/min

Mobile phase: (A) 0.1% FORMIC ACID IN WATER, (B) ACN

Gradient: T/%B 0/5,1/5, 6/100, 8/100, 10/5, 12/5

Column Temperature: 40 °C

Rt: 7.03 min, 98.36%

^{1}H NMR (400 MHz, DMSO-*d6*) δ 10.82 (s, 1H), 10.43 (s, 1H), 7.87 – 7.81 (m, 2H), 7.76 – 7.67 (m, 4H), 7.64 (dd, *J* = 9.1, 7.1 Hz, 1H), 7.46 – 7.39 (m, 1H), 7.37 – 7.32 (m, 1H), 7.10 – 7.03 (m, 2H), 3.79 (s, 3H).

^{13}C NMR (101 MHz, DMSO-*d6*) δ 165.6, 162.5, 149.6, 145.6, 138.4, 134.7, 133.5, 130.9, 129.3, 128.9, 126.7, 123.1, 123.0, 122.0, 119.5, 114.5, 111.8, 55.6.

HRMS (ESI) *m/z* calculated for $C_{20}H_{17}N_4O_5S^+$ $[M+H]^+$ 425.0914, found 425.0904.

Synthetic scheme for N-(benzo[c][1,2,5]oxadiazol-4-yl)-4-(trifluoromethyl)benzamide (4)

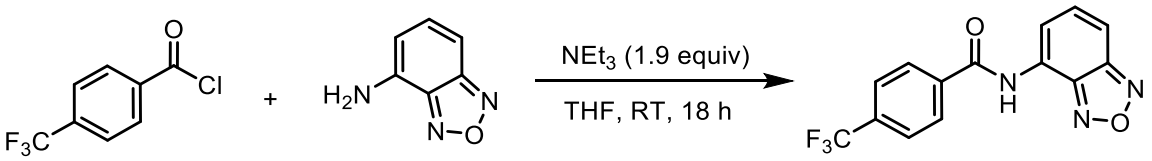

Synthesis of N-(benzo[c][1,2,5]oxadiazol-4-yl)-4-(trifluoromethyl)benzamide (4)

To a solution of benzo[c][1,2,5]oxadiazol-4-amine (51 mg, 0.38 mmol, 1.0 equiv) in THF (1.75 mL) in a 10 mL glass vial was added 4-(trifluoromethyl)benzoyl chloride (100 mg, 0.48 mmol, 1.25 equiv) followed by triethylamine (73 mg, 0.72 mmol, 1.9 equiv). The resulting mixture was shaken in a shaker for 18 hours. Then, the mixture was filtered and concentrated *in vacuo*. The residue was re-dissolved in methanol/acetonitrile (3 mL) and directly subjected to purification by HPLC. The product-containing fractions were pooled and concentrated *in vacuo* to furnish N-(benzo[c][1,2,5]oxadiazol-4-yl)-4-(trifluoromethyl)benzamide (**4**) (50 mg, 0.16 mmol, 43% yield) as a light yellow solid.

^{1}H NMR (400 MHz, DMSO-*d6*) δ 11.15 (s, 1H), 8.23 – 8.18 (m, 2H), 7.98 – 7.93 (m, 3H), 7.88 – 7.85 (m, 1H), 7.67 (dd, *J* = 9.1, 7.1 Hz, 1H).

^{13}C NMR (101 MHz, DMSO-*d6*) δ 165.2, 149.6, 145.6, 137.5, 133.5, 131.7 (q, *J* = 32.2 Hz), 129.0, 126.4, 125.5 (q, *J* = 3.7 Hz), 123.9 (d, *J* = 272.8 Hz), 122.2, 112.1.

^{19}F NMR (377 MHz, DMSO-*d6*) δ –61.4.

HRMS (ESI) *m/z* calculated for $C_{14}H_9F_3N_3O_2^+$ $[M+H]^+$ 308.0641, found 308.0650.

^{1}H NMR spectrum of compound 1 in DMSO-*d6*

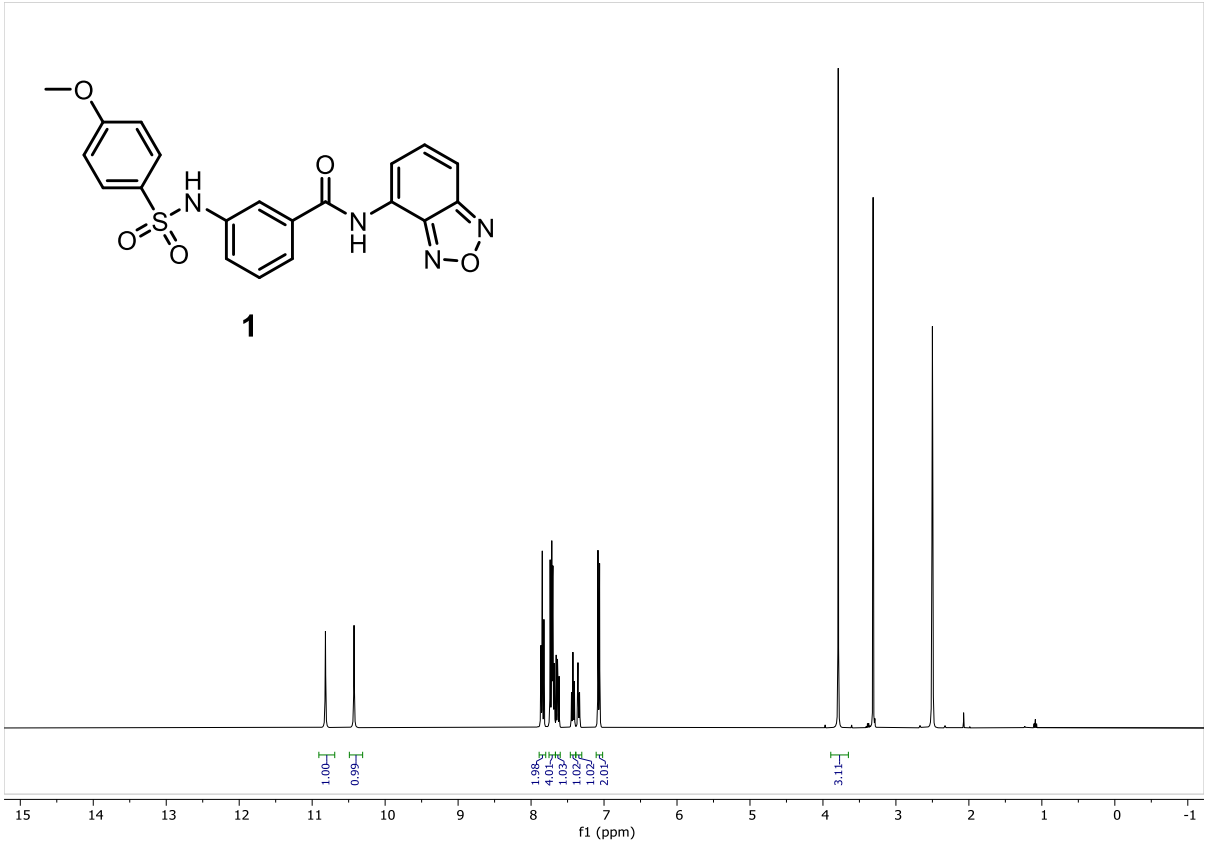

^{13}C NMR spectrum of compound 1 in DMSO-*d6*

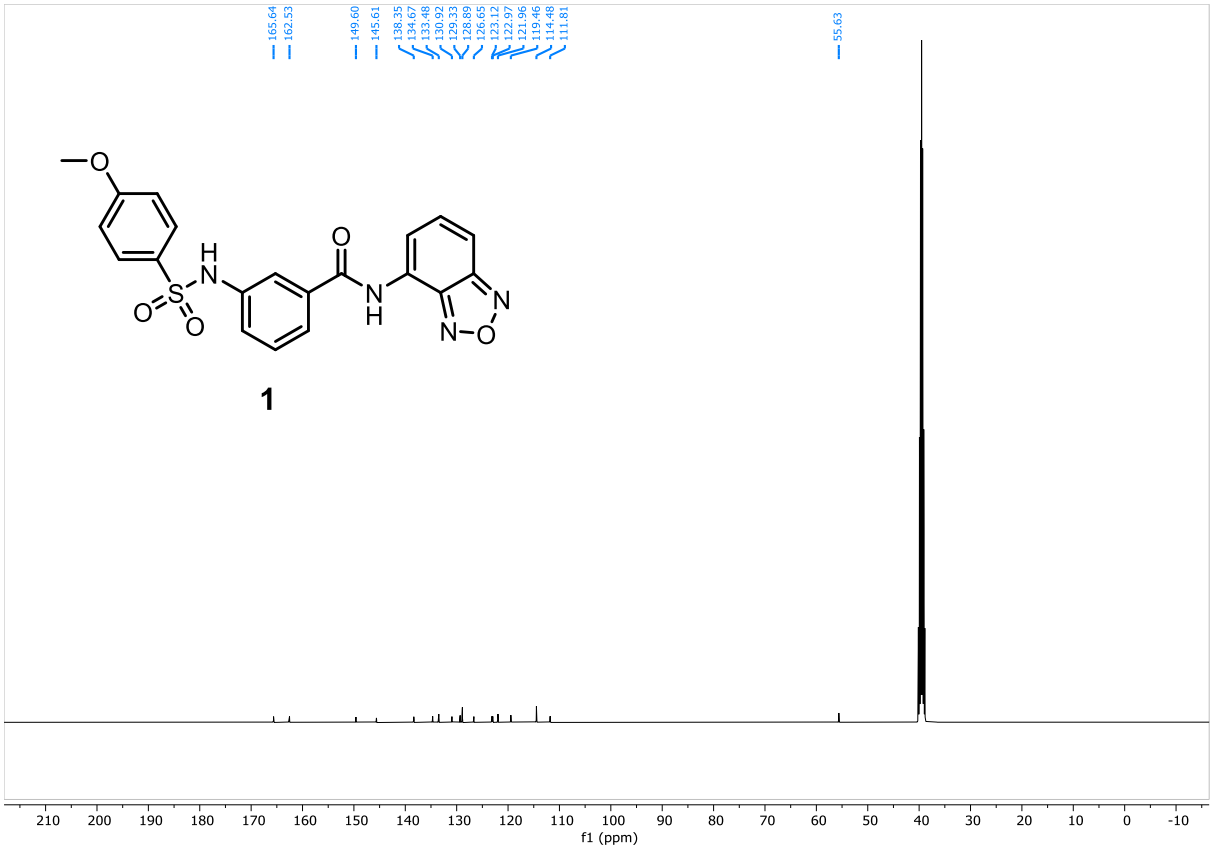

^{13}C NMR spectrum of compound 1 in DMSO-*d6* (zoomed in)

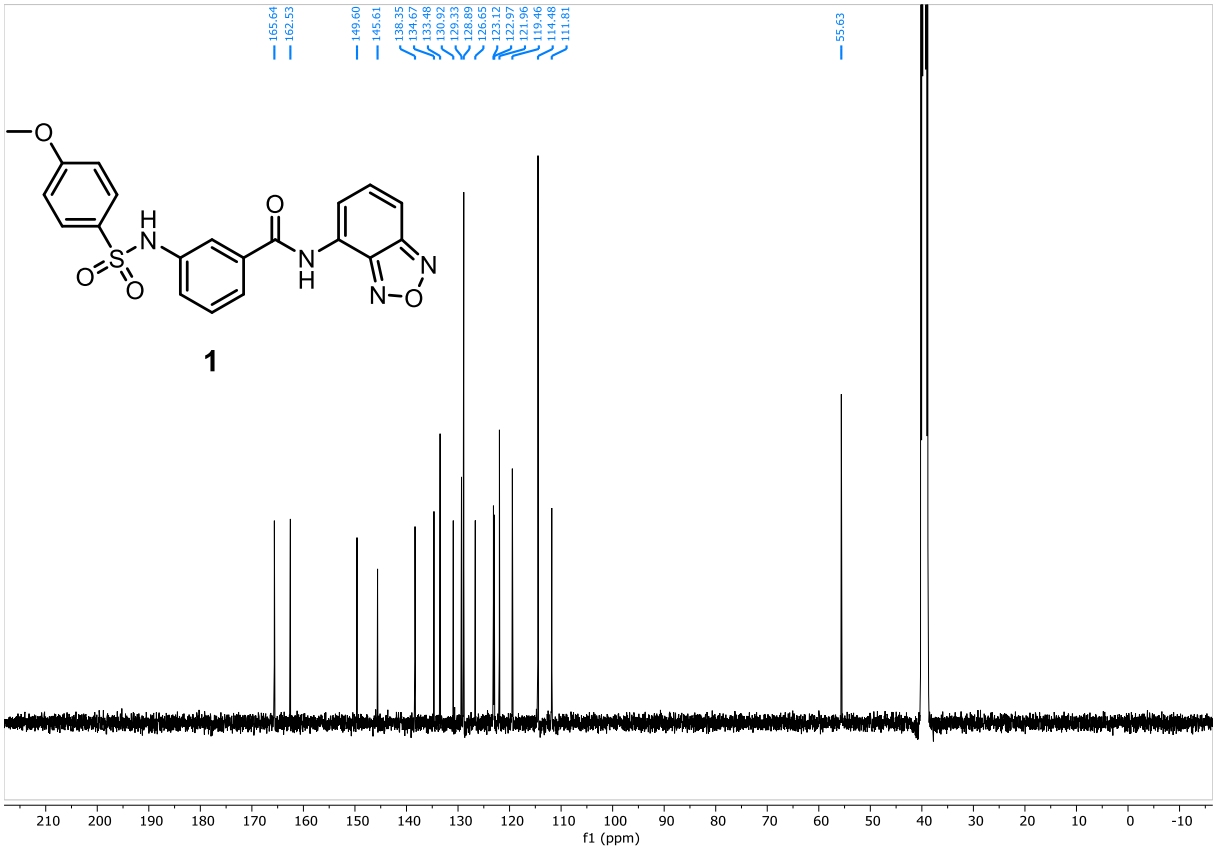

^{1}H NMR spectrum of compound 4 in DMSO-*d6*

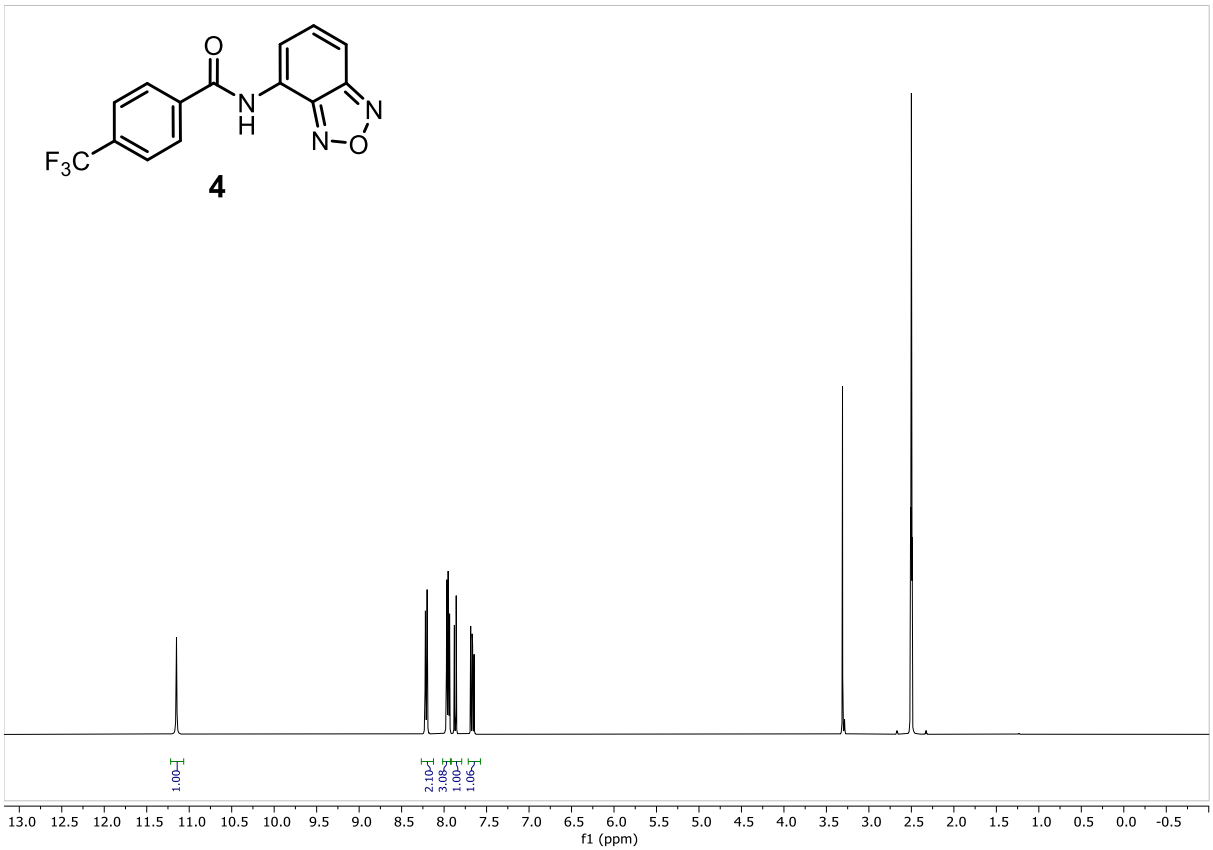

^{13}C NMR spectrum of compound 4 in DMSO-*d6*

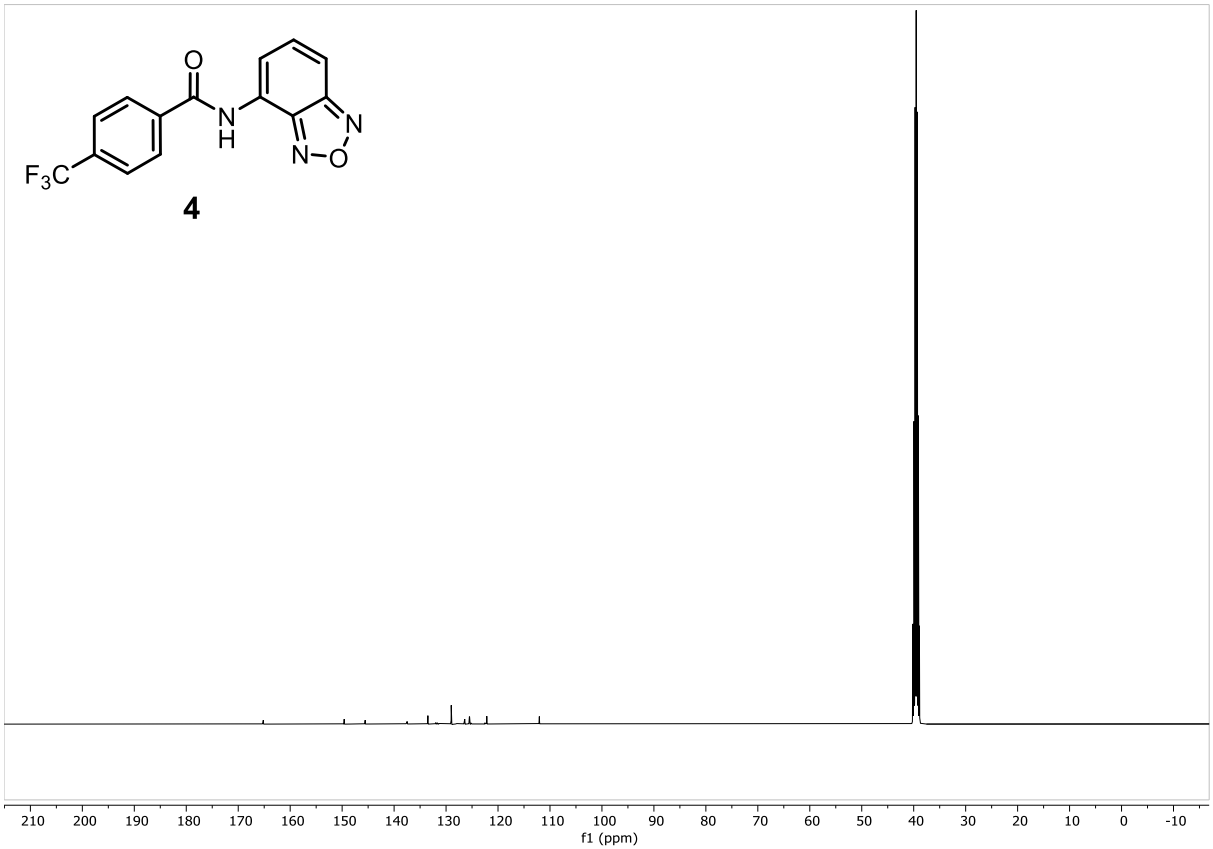

^{13}C NMR spectrum of compound 4 in DMSO-*d6* (zoomed in)

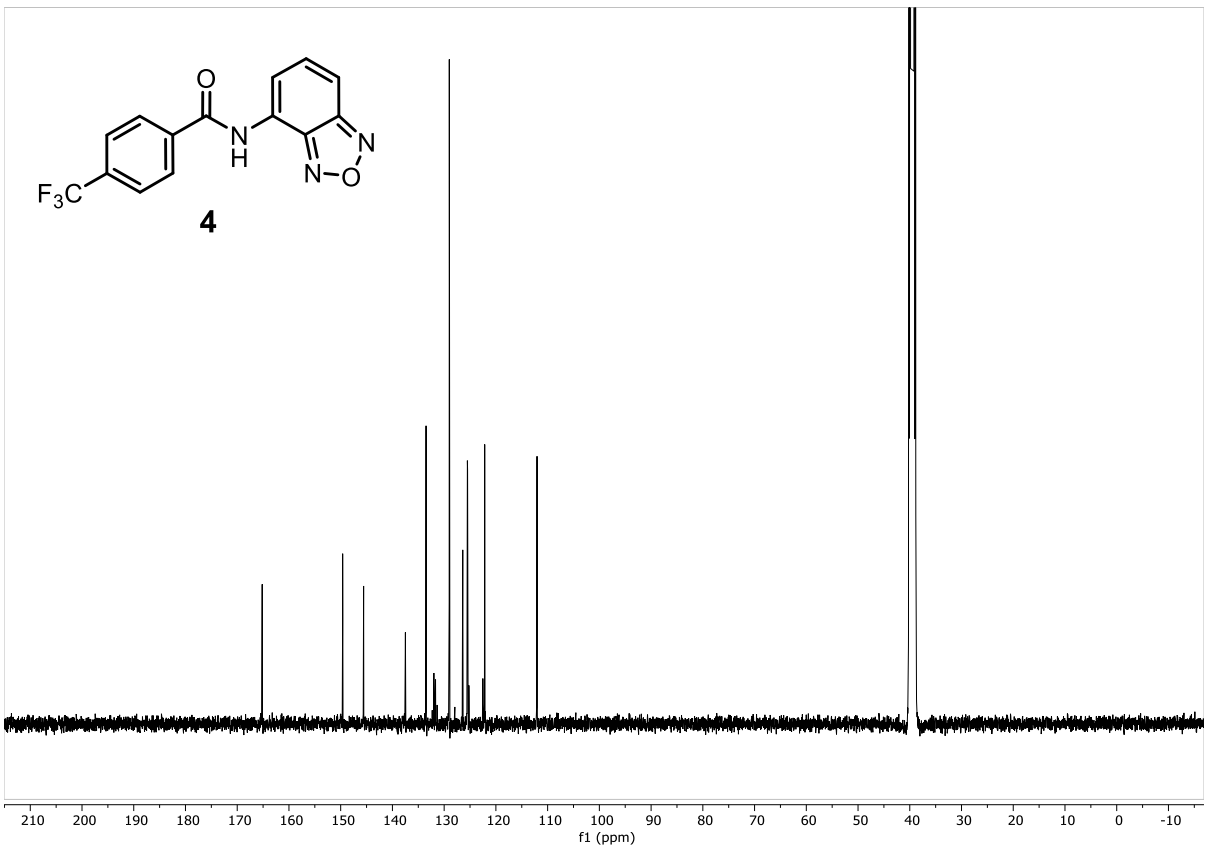
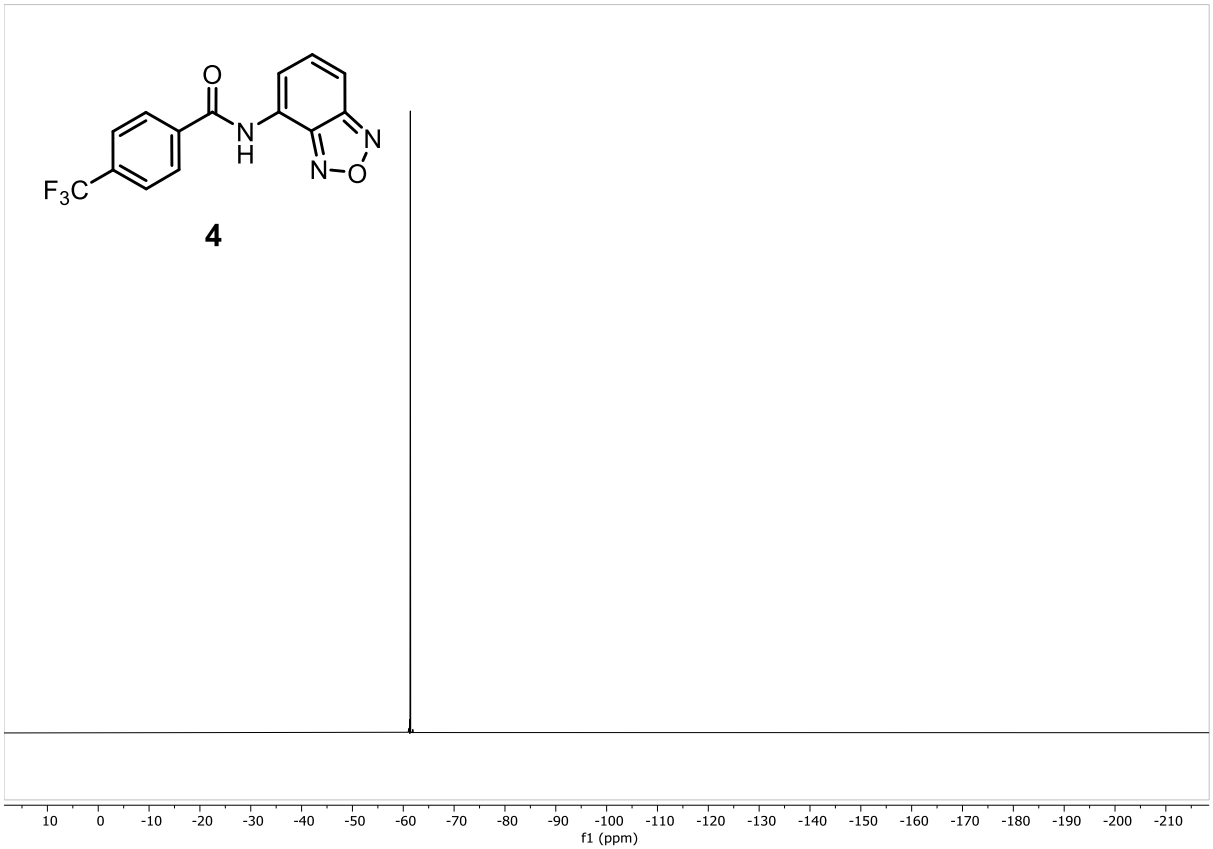
^{19}F NMR spectrum of compound 4 in DMSO-*d6*